- 1 Modelling of Cardiac Biventricular Electromechanics with Coronary
- 2 Blood Flow to Investigate the Influence of Coronary Arterial Motion on
- **3** Coronary Haemodynamic
- 4 Laila Fadhillah Ulta Delestria, Amr Al Abedb, Socrates Dokosb, Mohd Jamil Mohamed
- 5 Mokhtarudin<sup>c</sup>, Foo Ngai Kok<sup>d</sup>, Neil W Bressloff<sup>e</sup>, Bram G Sengers<sup>f</sup>, Azam Ahmad Bakir<sup>a,\*</sup>
- 6 <sup>a</sup>Smart Manufacturing and Systems Research Group, University of Southampton Malaysia,
- 7 79100 Iskandar Puteri, Johor, Malaysia.
- 8 bGraduate School of Biomedical Engineering, University of New South Wales, Sydney,
- 9 Australia.
- 10 °Centre for Research in Advanced Fluid and Processes (Fluid Centre), Universiti Malaysia
- 11 Pahang Al-Sultan Abdullah, Lebuhraya Tun Razak, 26300 Kuantan, Pahang, Malaysia.
- d Carbon Neutrality Research Group, University of Southampton Malaysia, 79100 Iskandar
- 13 Puteri, Johor, Malaysia.
- <sup>e</sup>School of Mechanical Engineering, Faculty of Engineering and Physical Sciences, University
- of Leeds, Leeds, United Kingdom.
- <sup>f</sup>Faculty of Engineering and Physical Sciences, University of Southampton, Southampton,
- 17 United Kingdom.
- 18 Corresponding author\*
- 19 Azam Ahmad Bakir (a.ahmad-bakir@soton.ac.uk)
- 20 Smart Manufacturing and Systems Research Group, University of Southampton Malaysia,
- 21 79100 Iskandar Puteri, Johor, Malaysia

# Highlights

- A computational model framework coupling a 3D biventricular electromechanics to a 3D coronary circulation
  - Integrate core elements of cardiac electromechanical model including cardiac fibre orientation, electrophysiology, active force and myocardial mechanics with coronary blood dynamics model using a simplified one-way coupling approach
    - Presents the significance of cardiac-induced motion of coronary arteries on the coronary haemodynamic
    - The framework model advances the understanding of the significance of incorporating background cardiac motion on coronary haemodynamic in computational models of cardiology and provides a basis for modelling myocardial perfusion in the investigation of coronary artery diseases

#### Abstract

- **Background and Objective:** Coronary flow is strongly influenced by the geometry and motion of coronary arteries, which change periodically in response to myocardial contraction throughout the cardiac cycle. However, a computational framework integrating cardiac biventricular electromechanics with dynamic coronary artery flow using a simplified, yet comprehensive mathematical approach remains underexplored. This study aims to develop a coupled 3D model of cardiac biventricular electromechanics and coronary circulation, enabling simulation of the interplay between cardiac electrical activity, mechanical function and coronary flow.
- **Methods:** A patient-specific biventricular electromechanical model encompasses the fibre orientation, electrophysiology, mechanical properties and an open-loop heart circulation is developed. The electromechanical model is simulated independently from the coronary circulation model. The model provides an input for the Navier-Stokes-based coronary flow model. A one-way coupling approach maps the biventricular motion to the coronary arteries, linking both components. To evaluate the influence of coronary arterial motion on coronary haemodynamic, simulations are performed for two scenarios: a moving and a non-moving (static) coronary artery model.
- Results: Cardiac-induced coronary motion alters the pressure, velocity and flow profiles. Nonmoving coronary arteries produce stable counter-rotating Dean-like vortices due to steady flow

55	curvature changes disturb the flow. Coronary motion significantly affects the wall shear stress,
56	highlighting the necessity of incorporating arterial dynamics to investigate atherosclerosis.
57	Conclusion: The integrated biventricular-coronary model emphasizes the significance of
58	background cardiac motion in coronary haemodynamic. The model offers a foundation for
59	exploring myocardial perfusion mechanisms in realistic physiological settings.
60	Keywords
61	Cardiac electromechanics, Cardiac-coronary coupling, Cardiac motion, Coronary blood flow,
01	Cardiac electroniechanics, Cardiac-coronary coupling, Cardiac motion, Coronary blood now,
62	Myocardial perfusion
63	

dominated by centrifugal forces, while the moving arteries disrupt these vortices as arterial

## 1.0 Introduction

Cardiovascular diseases (CVD) continue to impact over half a billion people worldwide, accounting for nearly one-third of all global deaths [1]. Coronary artery disease (CAD) is listed as among the most prevalent and life-threatening cardiovascular conditions with approximately 1 in 20 adults aged 20 and older suffering from CAD [2, 3]. CAD is primarily characterized by the narrowing or blockage of coronary arteries due to atherosclerosis, which restricts the blood flow to the heart muscle or myocardium reducing oxygen delivery for cardiac function. CAD can further progress to myocardial ischemia, a state of insufficient oxygenation of myocardial tissue that can impair cardiac function. If untreated, it can lead to severe heart complications including potentially fatal cardiac infarction or heart attack [4, 5]. Hence, understanding the physiology of coronary flow dynamics and factors influencing myocardial ischemia is crucial for diagnosing, treating and preventing adverse outcomes.

Coronary arteries undergo substantial motion during the cardiac cycle due to the anatomical attachment with the myocardium. Achenbach et al. [6] obtained data from 25 patients (mean age 59 years) who underwent cine electron-beam computed tomography (EBCT) for clinical reasons and had normal left ventricular (LV) function. This study acquired 20 consecutive cross-sectional images of the right coronary artery (RCA), left anterior descending (LAD) and left circumflex (LCX) coronary arteries. They found that the mean velocity of RCA movement was 69.5 mm/sec  $\pm$  22.5, which significantly faster than the LAD  $(22.4 \text{ mm/sec} \pm 4.1)$  and LCX  $(48.4 \text{ mm/sec} \pm 15.0)$ , showing that the RCA exhibits the most motion of the three arteries. Similarly, by using EBCT, these studies [7, 8] supported the previous work that RCA has the greatest motion followed by the LCX and LAD throughout a cardiac cycle. Ding and Friedman [9] analysed the motion parameters of human RCA and LAD arteries using biplane coronary angiograms. They found that the LAD experienced less displacement but exhibited more torsion than the RCA. This study also highlighted that coronary artery motion varies significantly among individuals and along the vessel axis, which contributes to differences in susceptibilities of each artery to atherosclerosis. Johnson et al. [10] examined 15 patients with CAD using bi-plane X-ray angiography and found that the LAD and LCX mostly move in the cranial-caudal plane while the RCA moves left-right direction. Besides, the maximum motion was seen in the mid-segments of the RCA (16.08 mm), LAD (6.07 mm) and the distal segment of the LCX (9.65 mm). In another study, Shechter et al. [11] obtained data from 10 patients (mean age  $65 \pm 11$  years) who were referred for diagnostic left heart catheterization, including four with mild dilated cardiomyopathy and two with mild to moderate hypertrophy. Using biplane angiograms, they reconstructed the RCA, LCX and LAD and tracked their motion with tracking techniques to measure the 3D displacement and velocity due to cardiac and respiratory motion. According to them, during cardiac contraction, all arteries moved leftward, inferiorly, and anteriorly with the RCA has the most displacement. The maximum 3D displacements were 14.4 mm for the RCA, 12.2 mm for the LCX and 9.6 mm for the LAD. Tan et al. [12] analysed selected computed tomography (CT) images from 17 patients (aged 18 to 70 years) who had undergone multi-slice CT-based coronary angiography with retrospective electrocardiogram (ECG) gating. All patients had suspected heart disease but no history of cardiac disease. The study measured coronary artery displacement finding that the RCA finding had the greatest displacement (4.5 - 6.2 mm) compared to the left main artery (3.9 – 4.5 mm), while the LAD, LCX and right marginal artery showed displacements ranging from 3.7 - 6.6 mm. The aforementioned studies demonstrated that imaging data revealed significant variations in coronary artery displacement and velocity across different arteries during cardiac cycles.

97

98

99

100

101

102

103

104

105

106

107

108

109

110

111

112

113

114

115

116

117

118

119

120

121

122

123

124

125

126

127

128

129

The contraction and relaxation of the heart influence the coronary blood flow and drive myocardial perfusion [13, 14]. Based on these studies' findings [9, 15-21], physiological coronary arterial motion can influence coronary haemodynamic affecting the pulsatility of the coronary flow. It affects the magnitudes of wall shear stress (WSS), pressure, flow characteristics, oscillatory shear index (OSI) and other haemodynamic metrics, potentially providing insights into plaque formation or other pathological changes. Low WSS and high OSI conditions are commonly associated with the initiation and progression of atherosclerosis [22-24]. Zeng et al. [20] have modelled a simple circular geometry of an RCA subject to a realistic cardiac motion to predict the effects on RCA haemodynamic. Their comparison of moving and stationary models showed that the dynamic RCA model predicted notable secondary flow patterns in terms of the size, strength and location of vortices. More importantly, the arterial movement generated larger WSS variations than the predicted stationary model, due to the changes in 3D curvature of the artery. Similar work was carried out by Torii et al. [21] with the findings predicted that models with dynamic vessel motion produce higher maximum WSS than the stationary model during peak systolic flow, middiastole and early systole, a similar observation to that seen by Zeng et al. [20]. Their study also demonstrated a wide area of high OSI within the moving RCA model which also marked

a high relative residence time (RRT). These comparable studies underscore the substantial role of coronary motion in modulating blood flow patterns within the coronary arteries.

While randomized clinical trials are the preferred method for understanding realistic cardiac behaviour, computational models in cardiology have garnered considerable interest as a non-invasive modality to understand mechanisms underlying cardiac diseases. Previous studies have conducted cardiac biventricular electromechanical modelling using subject-specific canine hearts [25] and a generic biventricular heart model [26]. Bakir et al. [27] have extended these works to develop a fully-coupled cardiac fluid-electromechanics finite element model of a generic human biventricular model. Regazzoni et al. [28] introduced a novel mathematical model of left ventricular electromechanics coupled with a lumped parameter of closed-loop heart circulation. These most recent studies [29-31] have proposed a comprehensive electromechanical model of the entire heart including the atrial contraction by coupling the 3D electromechanical model of the heart with 0D haemodynamic model of the circulatory system. These models capture the multiscale and multiphysics processes governing the cardiac function and the key components of such models are myocardial fibre architecture, cardiac electrophysiology, active and passive cardiac mechanics, and blood dynamics.

Integrating the cardiac electromechanical model with coronary flow dynamics forms an inclusive framework that encapsulates the physiology of human cardiac function. This coupling approach enables a more holistic representation of the heart's electrical, mechanical and haemodynamic and its interaction with coronary circulation. A few recent studies [32-35] have developed a cardiac-coronary modelling framework where they coupled the systemic circulation of the heart - mostly focusing on the LV with the coronary circulation typically using a 0D or 1D structured tree model. Recently, Wang and Yin [36] have developed a oneway coupling of a 3D LV finite element model with a 1D structured tree of coronary flow by considering the influence of time-varying intramyocardial pressure (IMP). To the best of our knowledge, Zingaro et al. [37] presented the first example of a comprehensive mathematical model in which a detailed 3D LV electromechanical model was combined with a Darcy multicompartment biventricular model to simulate myocardial perfusion. To be specific, they developed a fully coupled electromechanical model which serves as input for Navier-Stokes-Darcy model of the biventricular domain. However, their electromechanical heart simulation was restricted to the left side of heart solely. Their model did not incorporate fluid dynamics in the right side of heart, assuming no direct feedback of the right heart hemodynamic on

myocardial perfusion. Besides, they assumed active mechanics driven by electrophysiology were present only in the left ventricle thus the atria were treated as electrically passive material, as the study primarily focused on the downstream dynamics of the aortic valve. For the perfusion model, they employed a biventricular fixed domain approach (the domain is non-deformable) that they neglected the effect of tissue deformation on blood perfusion. One important limitation of their study was the assumption of zero displacement on the coronary walls that the coronary arteries remained fixed, for simplicity.

Based on the limitations of the previous works, there remains a need to develop a realistic and comprehensive computational heart model that considers the electromechanics of whole heart coupled with coronary arterial circulation. Studies should implement a deformable domain for perfusion modelling, in order to account for the effects of myocardial contraction on coronary blood flow by using poroelasticity model or moving myocardial boundary conditions. The dynamics of coronary artery, such as the coronary artery wall motion and its deformation must be considered instead of assuming a fixed geometry which is unrealistic when modelling the coronary blood flow. Therefore, this study proposes a framework to develop a computational myocardium-coronary coupling model combining 3D cardiac biventricular electromechanics with 3D coronary arterial flow dynamics to investigate the mechanisms of myocardium-coronary interaction. The contribution of this article follows two strands: (a) first, we present a multiphysics model of 3D biventricular cardiac electromechanics coupled with a computational fluid dynamics (CFD) model of 3D coronary artery, (ii) second, we show the significance of cardiac-induced coronary arterial motion on the coronary blood flow patterns.

#### 2.0 Methods

This study aims to develop a patient-specific biventricular electromechanical model coupled with a coronary flow model to investigate the influence of cardiac-induced coronary artery motion on coronary haemodynamic. Two cases were simulated: a moving coronary artery model and a non-moving coronary artery model. In the moving model, a one-way coupling framework was implemented, where the displacement of the coronary artery was set to match the displacement of the nearest myocardium. In the non-moving model, the coronary artery remains static throughout the cardiac cycle. In this methodology section, we first describe the mathematical formulation of the electromechanical model, including the geometrical domain, myocardial fibre orientation, electrophysiology, biventricular mechanics and the open-loop circulation model. Next, we explain the CFD model of the coronary artery. Then, we present a one-way coupling method used to link the biventricular electromechanical model with the coronary artery flow model. Lastly, we outline the solver settings employed to run the multiphysics model.

## 2.1 Geometrical domain

We acquired a pre-segmented patient-specific 3D model of the coronary arteries (Model ID: 0073\_H\_CORO\_H) from the Vascular Model Repository, an open-source database of cardiovascular models [38, 39]. The model was obtained from a high-resolution CT scan of a healthy 28-year-old female patient (see Figure 1 and Table 1 in Supplementary Materials I). The left coronary arteries (LCA) consist of a short stem referred to as the left main coronary artery which bifurcates into the two LAD arterial branches (LAD1 and LAD2) and four LCX arterial branches (LCX1, LCX2, LCX3 and LCX4). The RCA is divided into three branches (RCA1, RCA2 and RCA3). Since the coronary arteries were already segmented and provided as a 3D model, we have focused on segmenting the biventricular myocardium. Using 3D Slicer software (version 5.2) [40, 41], we segmented the left and right ventricular chambers, including the epicardial and endocardial contours of the myocardium from the CT images. The detailed explanation of the segmentation process was shown in Supplementary Materials I (see Figure 2 in Supplementary Materials I). Figure 1 (A) depicts the 3D computational model of the biventricular myocardium and coronary artery. The biventricular domain, Ω<sub>domain</sub> incorporated anatomical features of both ventricles and was partitioned into the left and right

epicardium,  $\Omega_{epi,LV}$  and  $\Omega_{epi,RV}$ , left and right endocardium,  $\Omega_{endo,LV}$  and  $\Omega_{endo,RV}$ , biventricular apex,  $\Omega_{apex}$  and basal,  $\Omega_{base}$  as shown in **Figure 1 (B)**. To avoid potential convergence issues arising from the complexity of meshing and solving multiphysics problems, we opted to treat the coronary artery and biventricular myocardium as distinct components with their respective dynamics handled independently before being coupled using a data mapping.

221

222

223

224

225

226

227

228

229

230

231

232

233

234

235

236

237

238

239

240

241

242

216

217

218

219

220

### 2.2 Myocardial fibres

The microstructure of the myocardium is composed of myofibers oriented in fibre, sheet and normal-to-sheet directions. Since fibres arrangement primarily determines the direction for conduction of electrical signals and passive mechanical properties [42], the orientation of the fibres produce anisotropic conduction [43]. Specifying a proper fibre orientation within the myocardium is essentially a first line task in computational heart modelling to obtain accurate simulations. To prescribe the fibre architecture in the biventricular surface domain, we implemented a Laplace-Dirichlet Rule-Based Method (LDRBM), widely reported in the literatures [27, 44-46]. In this work, the following assumptions were made for simplicity: (a) the fibre orientations were assumed to vary transmurally at an angle of -60° with respect to circumferential axis at the epicardium and +60° at the endocardium [47, 48] and, (ii) the sheets were assumed to lie perpendicular to both the epicardial and endocardial surfaces. Using the LDRBM method, we defined a transmural distance,  $\phi_{transmural}$  that is from the epicardium to the endocardium and an apicobasal distance,  $\phi_{apicobasal}$  that is from the base to the apex of the biventricular domain as the solutions to the Laplace boundary problems. Based on the transmural and apicobasal distances, we assigned local base tangent vectors,  $[\hat{\boldsymbol{e}}_{l}, \hat{\boldsymbol{e}}_{n}, \hat{\boldsymbol{e}}_{c}]$  at each point of the biventricular domain, respectively representing the longitudinal, normal and circumferential directions. This reference frame,  $[\hat{e}_l, \hat{e}_n, \hat{e}_c]$  was then rotated accordingly to define the myocardial microstructural orientations,  $[\hat{e}_l, \hat{e}_n, \hat{e}_c] \rightarrow [\hat{f}_0, \hat{s}_0, \hat{n}_0]$  where  $\hat{f}_0$  is the fibre,  $\hat{s}_0$  is the sheet and  $\hat{n}_0$  is the normal-to-sheet directions. Figure 1 (C) presents the developed myocardial fibre architecture showing the helical structure within the ventricles.

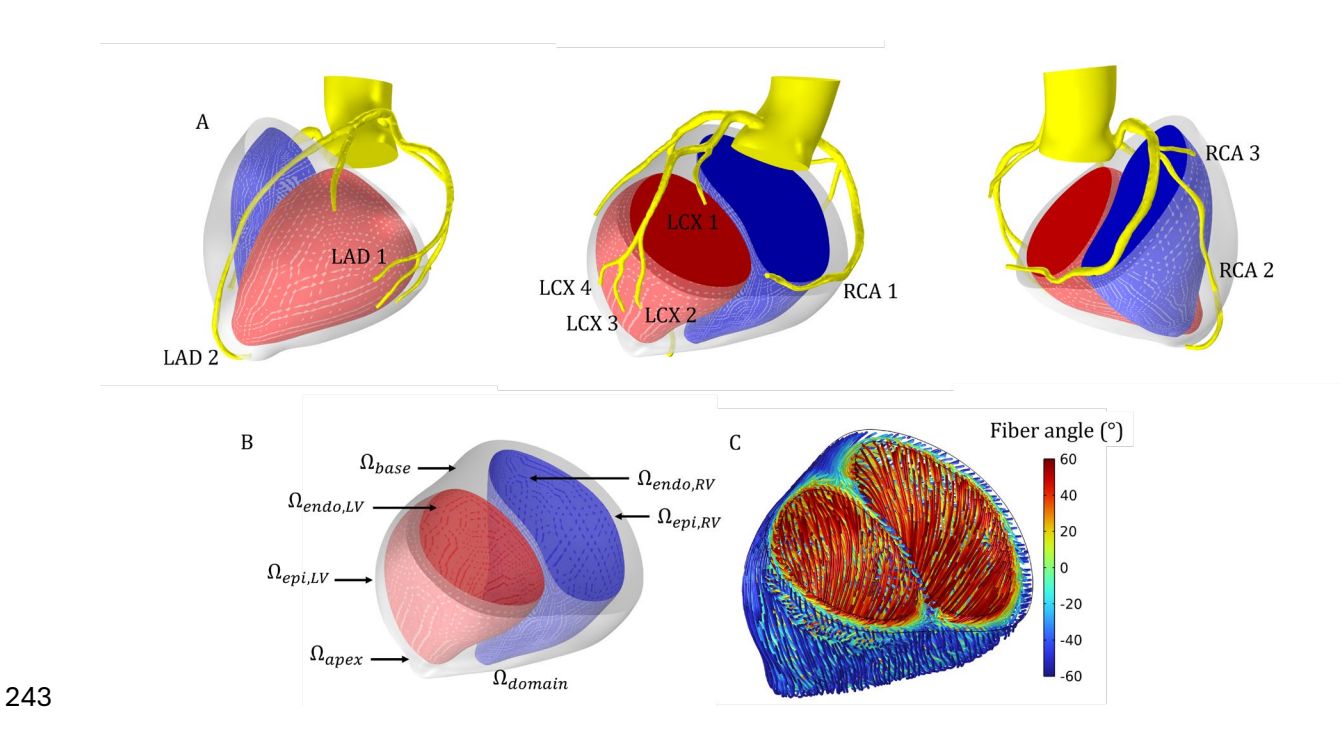


Figure 1 (A, B) Computational domains of the biventricular myocardium and coronary artery model. Colours and labels denote the partitions of the domain boundaries and naming of each artery. (C) Biventricular fibres orientation

## 2.3 Cardiac electrophysiology

# 2.3.1 Action potential

The cardiac action potential formulations were described in Eqs. (1)-(3) based on previous works [27, 49, 50]. Eq. (1) represents the transmembrane potential dynamics  $(V_m)$  and action potential propagation within the myocardium. Eq. (2) indicates the transmembrane ionic current flow  $(i_{ion})$  while Eq. (3) governs the recovery of the action potential in the myocardium (R). Value and description of the parameters setting are listed in Table 1.

254 
$$\beta \left( C_m \frac{\partial V_m}{\partial t} + i_{ion} \right) = \nabla_X \cdot (\boldsymbol{\sigma} \nabla_X V_m)$$
 (1)

255 
$$i_{ion} = k_1 k_2 (V_m - B) \left( \left[ \frac{V_m - B}{A} - a \right] (V_m - 1) + k_2 R (V_m - B) \right)$$
 (2)

256 
$$\frac{\partial R}{\partial t} = \left(\varepsilon_0 + \frac{\mu_1 R}{\left(\frac{V_m - B}{A} + \mu_2\right)} \left(-R - k_1 \left(\frac{V_m - B}{A}\right) \left(\left(\frac{V_m - B}{A}\right) - a - 1\right)\right)\right)$$
(3)

Parameter	Values	Description	
β	160000 m <sup>-1</sup>	Membrane surface to volume ratio of the myocardial tissue	
$C_m$	0.01 F m <sup>-2</sup>	Membrane capacitance per unit area	
$V_m$		Myocardial membrane potential	
$i_{ion}$		Ionic current density	
σ		Electrical conductivity tensor	
$\nabla_X V_m$		Diffusion term to represent the spread of the electrical potential within the myocardial tissue	
$k_1$	8	Constants related to the rate of the ionic currents	
$k_2$	100 s <sup>-1</sup>	Constants related to the rate of the folia currents	
В	-0.08 V	Constant that shifts the baseline of the transmembrane potential	
A	0.1 V	Scaling factor to adjust the sensitivity of the ionic current	
а	0.12	Unitless constant governing the action potential duration	
R		Recovery variable	
$arepsilon_0$	$0.2 \text{ s}^{-1}$	Baseline rate of recovery	
$\mu_1$	20 s <sup>-1</sup>	Constants that modulate the recovery rate	
$\mu_2$ 0.3		Constants that modulate the recovery rate	
Initial values			
$V_m$ -0.08 V		Myocardial membrane potential	
R	R 0.02 Unitless recovery variable		

## 2.3.2 Electrical conductivity tensor

The cardiac cells' electrical conduction travels the fastest along the fibre direction and the slowest in the direction perpendicular to the muscle fibre [51-53]. This rapid conduction enables a coordinated contraction of the ventricles for efficient ventricular contraction and effective ejection of blood. For this work, the electrical conductivity of the myocardium was set to exhibit the anisotropic properties at a ratio of 4:2:1 along the fibre  $(\hat{F})$ , sheet  $(\hat{S})$  and normal-to-sheet  $(\hat{N})$  directions, respectively based on prior studies [53, 54]. Eq. (4) describes the conductivity tensor,  $\sigma$  according to the conductivities in the direction of fibres  $(\sigma_f)$ , sheets  $(\sigma_s)$  and normal-to-sheets  $(\sigma_n)$ 

269 
$$\sigma = \sigma_f(\hat{F} \otimes \hat{F}) + \sigma_s(\hat{S} \otimes \hat{S}) + \sigma_n(\hat{N} \otimes \hat{N})$$
 (4)

270 with  $\sigma_f = 3 \text{ S m}^{-1}$  and  $\otimes$  denotes the vector outer product.

## 2.4 Myocardial mechanics

#### 2.4.1 Active stress

In response to the action potential, the biventricular myocardium generates an active stress. We utilized a simplified version of the active stress formulation, see Eq. (5) proposed by Bakir et al. [27]

276 
$$\frac{\partial T_a}{\partial t} = \epsilon(V_m) \left( k_{Ta} \left( \frac{V_m - B}{A} \right) - T_a \right)$$
 (5)

where  $T_a$  is the active stress representing the contractile force generated by the myocardium and  $k_{Ta}$  is a parameter controlling the magnitude of the active stress. The delay function,  $\epsilon(V_m)$  models the rate at which active stress develops in response to the changes in the transmembrane potential and the equation is taken from Göktepe and Kuhl [26] as shown in Eq. (6). Value and description of the parameters setting are listed in Table 2.

282 
$$\epsilon(V_m) = \epsilon_0 + (\epsilon_\infty - \epsilon_0) exp(-exp(-\xi(V_m - V_{threshold})))$$
 (6)

Table 2 Parameters and initial value of the myocardial contraction – excitation formulations

Parameter	Values	Description	
$k_{Ta}$	253 kPa	Parameter controlling the magnitude of the active stress	
$\epsilon_0$	5.7 s <sup>-1</sup> Baseline rate of the active stress generation		
$\epsilon_{\infty}$	28 s <sup>-1</sup>	Maximum rate of the active stress generation as $V_m$ increases well above the excitation threshold	
$\xi$ 7.6 V <sup>-1</sup>		Scaling factor	
V <sub>threshold</sub> -0.03 V		Threshold transmembrane potential at which the active stress generation rate begins to increase significantly	
Initial value			
$T_a$ 0 kPa		Active stress	

#### 2.4.2 Passive and active mechanics

The passive myocardial material response is important to determine the performance of mechanical contraction and relaxation that shapes the cardiac function. In this work, the passive behaviour of the myocardium was described by a hyper elastic model as proposed by the constitutive model from Holzapfel and Ogden [55]. It is assumed the myocardium exhibits nonlinear hyper elastic, incompressible and is locally transversely isotropic with respect to the fibre axis. Eqs. (7)-(9) defines the total strain energy density function,  $\psi$  decomposed into separate components to capture the mechanical properties of the myocardium

$$\boldsymbol{\psi} = \psi_{isotropic} + \psi_{fiber} + \psi_{vol}$$

295 
$$\psi_{isotropic} = \frac{a_i}{2b_i} exp(b_i(I_1 - 3) - 1)$$
 (7)

296 
$$\psi_{fiber} = \frac{a_f}{2b_f} exp\left(b_f (I_{4f} - 1)^2 - 1\right)$$
 (8)

297 
$$\psi_{vol} = \frac{k(J-1)ln(J)}{2}$$
 (9)

where  $\psi_{isotropic}$  represents the strain energy due to the myocardial's isotropic properties, 298  $\psi_{fiber}$  represents the strain energy due to the anisotropic behaviour of the fibres and  $\psi_{vol}$ 299 represents the volumetric strain energy due to deformation. Value and description of the 300 parameters setting are listed in Table 3.  $I_1$  is the first invariant of the modified right Cauchy-301 Green deformation tensor, **C** given  $I_{4f} = \hat{F} \cdot (\mathbf{C}\hat{F})$  is the fourth invariant of the right Cauchy-302 Green deformation tensor representing the anisotropic invariants associated with the fibre 303 directions and J represents the determinant of the deformation gradient tensor, F. To ensure 304 material stability,  $I_{4f}$  was set to 0 when  $I_{4f} < 0$ , to account for the assumption that myocardial 305 306 fibres do not contribute significantly to passive mechanics during compression. For the active myocardial mechanics, the active stress,  $T_a$  was added to the second Piola-Kirchhoff stress 307 tensor, T in the directions of fibre, sheet and normal-to-sheet as shown in Eq. (10) to couple 308 the electrical and mechanical formulations. The magnitude of the active stress in sheet and 309 normal-to-sheet directions is equal to 40 % of the stress magnitude perceived along the fibre 310 311 direction [54]. E denotes the Green-Lagrange strain tensor.

312 
$$T = \frac{\partial \mathbf{E}}{\partial t} + T_a(\hat{F} \otimes \hat{F}) + 0.4T_a(\hat{S} \otimes \hat{S}) + 0.4T_a(\hat{N} \otimes \hat{N})$$
 (10)

The equation of motion governing the myocardial deformation is given by Eq. (11)

$$314 0 = \nabla \cdot (\mathbf{FT})^T (11)$$

315  $\mathbf{F} = I + \nabla \mathbf{u}$ 

where  $\mathbf{F} =$  deformation of gradient tensor and  $\mathbf{u}$  is the myocardial displacement vector.

Table 3 Parameters value of the myocardial mechanics formulations

Parameter	Values	Description	
$a_i$	2.280 kPa	Parameters for the isotropic material properties	
$b_i$	9.726	Farameters for the isotropic material properties	
$a_f$	1.685 kPa	Donous atoms for the fibre studie meatonicle mean artiss	
$b_f$	15.779	Parameters for the fibre strain material properti	
k	250 kPa	Bulk modulus	

320

321

322

323

324

325

326

327

328

329

330

331

332

333

334

335

336

337

338

339

340

341

342

343

344

345

To note, the biventricular base at the top is assumed to be fixed, avoiding translation and rotation while other myocardial boundaries are allowed to move freely. We acknowledged that this differs from the physiological motion pattern, where the base moves more prominently [56]. However, our primary focus is on understanding the influence of myocardial motion on large coronary artery hemodynamic. The myocardial deformation field still captures key global contraction and expansion characteristics as shown in a previous work by Bakir et al. [27], allowing us to analyse how background motion affects coronary flow. To investigate potential impact of changing fixed reference frame, we performed an additional simplified simulation in a simple muscle slab with a curved cylindrical artery attached. We tested two cases: one with top wall fixed and the bottom wall moving (as in our original model) and another with the bottom wall fixed and the top wall moving (see Supplementary Materials II). The simulation results reveal that the location of the moving boundary – whether the top or bottom wall of the slab domain, has an overall similar spatiotemporal pattern with the same order of magnitude in the flow trends across the curved cylinder segment. In both cases, the maximum velocity is consistently observed at the top of the curved cylinder (3.8 m/s) for both cases. However, slight differences in the peak velocity values are shown at the mid and bottom sections of the curved cylinder between both cases. We noted minor phasic variations in the waveform between t =0.2 s and t = 0.4 s at both cases, likely due to the difference in the reference planes of both models. During this period, coinciding with the motion activation profile, the velocity peaks differently likely due to difference in motion direction. Similar minor phasic variation was also noted in the pressure where the fixed top wall case shows higher overall pressure magnitudes than the case of fixed bottom wall across the curved cylinder. While the outcomes suggest the point of reference can alter flow behaviour, albeit at minor variations, the general flow behaviour is largely unaffected. Although fixing base is more physiologically correct, however, this necessitates complex interactions with the atrial chambers to obtain correct basal motion. Therefore, based on the acquired geometrical domain of the biventricular model, fixing the base while permitting greater motion at the apex simplifies the computational process in our study.

## 2.5 Open loop circulation model

346

347

348

349

350

351

352

353

354

355

356

357

358

359

360

361

362

363

364

365

366

367

368

An open-loop 0D lumped parameter (three-element Windkessel) model [27] was prescribed at the electromechanical setting of the biventricular model to represent the heart circulatory system. This simplified approach captures the overall haemodynamic behaviour of the resistance and compliance of the circulatory system, thus governing the effect on ventricular pressures during ejection phase. Unlike closed-loop, the open-loop assumption is simpler but has several limitations such as producing unequal stroke volumes between the left and right ventricles which can compromise accurate simulation of real physiological conditions and lacks feedback mechanisms [27-29, 57] that regulate the heart function. But since the focus of this study is on the coupling between the myocardial mechanics and coronary haemodynamic, the open-loop assumption is sufficient for the purpose of setting up our computational framework, and a closed loop setup can be considered in the future. Using the lumped parameter model, the heart's circulatory system was modelled with a combination of resistances and capacitances in a circuit illustrated in Figure 2, represented by a system of ordinary differential equations (ODEs) expressed by Eqs. (12)-(17) in Supplementary Materials I that includes the pressures, volumes, and fluxes of each ventricular chamber. To note, in this cardiac electromechanical simulation study, blood hemodynamic is not explicitly modelled so the Navier-Stokes equation is absent in the ventricular cavities. Instead, the ventricular pressures were determined using Eqs. (18)-(21), allowing the model to replicate all phases of cardiac cycle. Ventricular volumes are obtained by integrating the ventricular chamber volume at each time step.

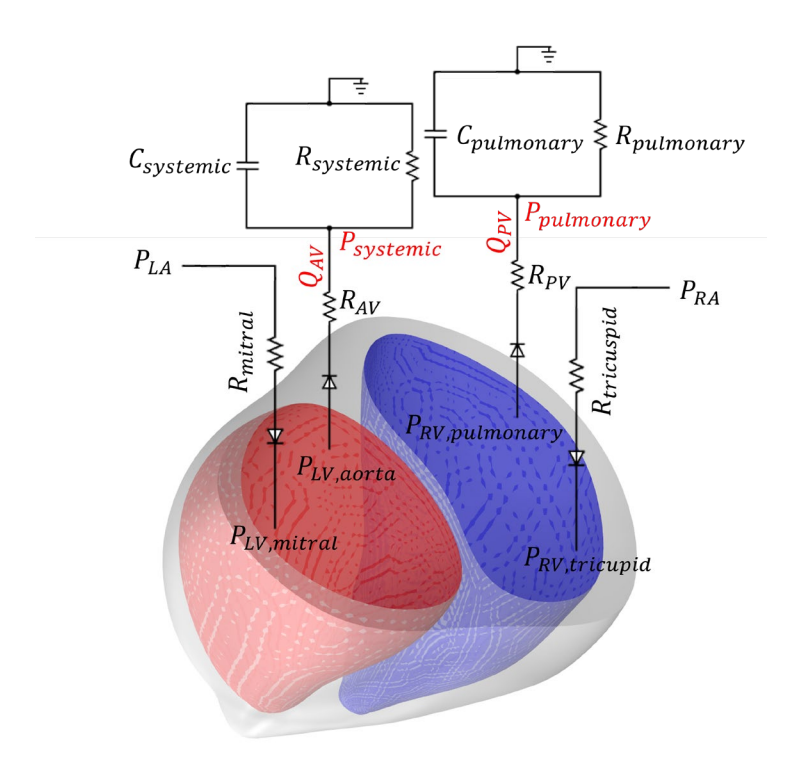


Figure 2 Biventricular open loop lumped parameter to model the heart circulation

The inlet of each ventricle was coupled with a passive atrium. The left atrium (LA) was initially assumed to be a constant pressure source of 16 mmHg while the right atrium (RA) was set to 7 mmHg. Based on the governing ODEs, the inlets of the LV and RV were prescribed with flowrates representing the flow through a mitral valve from the LA and a tricuspid valve from the RA, respectively. For the outlet conditions, flowrates governed by a three-element Windkessel model were implemented to simulate the systemic and pulmonary circulations. All parameters [27, 49] and initial variables for the ODEs are listed in **Table 4**.

Table 4 Parameters and initial values of the ODEs for the biventricular open loop circulation model

Parameter Values		Description	
$P_{LA}$	16 mmHg	Left atrial pressure	
$R_{mitral}$	0.7199 MPa.s/m <sup>3</sup>	Mitral resistance	
$R_{AV}$	7.9993 MPa.s/m <sup>3</sup>	Aortic resistance	
$C_{systemic}$	5.81 ml/mmHg	Systemic capacitance	
$R_{systemic}$	166.653 MPa.s/m <sup>3</sup>	Systemic resistance	
$P_{RA}$	7 mmHg	Right atrial resistance	
$R_{tricuspid}$	0.18 MPa.s/m <sup>3</sup>	Tricuspid resistance	
$R_{PV}$	1.9998 MPa.s/m <sup>3</sup>	Pulmonary resistance	
$C_{pulmonary}$	1.4525 ml/mmHg	Pulmonary capacitance	
$R_{pulmonary}$	41.6632 MPa.s/m <sup>3</sup>	Pulmonary resistance	
	itial values		
$P_{systemic}$	90 mmHg	Systemic pressure	

Parameter	Values	Description
$P_{pulmonary}$	90 mmHg	Pulmonary pressure

The electromechanical simulation was started by expanding the biventricular chamber from its zero-stress state increasing the LV volume from 77 ml to 118 ml at a pressure of 90 mmHg and the RV volume from 68 ml to 89 ml at a pressure of 10 mmHg. Inflow is introduced using a ramp function over 0-50 milliseconds to allow the flow to increase gradually from 0 ml/s, facilitating the model's convergence from its initial state. During this filling phase, both initial value of the Windkessel parameters,  $P_{systemic}$  and  $P_{pulmonary}$  were set to 90 mmHg. The left and right ventricular pressures during the isovolumic phases were determined as shown in Eq. (18) and (19) based on this literature [58]

389 
$$P_{LV,iso} = P_{LV,0} + k(V_{LV,0} - V_{LV})$$
 (18)

where  $P_{LV,iso}$  is the isovolumic pressure in the LV,  $P_{LV,0}$  is the reference or baseline pressure of the LV, k is a constant proportionality,  $V_{LV,0}$  is the initial volume of the LV and  $V_{LV}$  is the current volume of the LV and

393 
$$P_{RV,iso} = P_{RV,0} + k(V_{RV,0} - V_{RV})$$
 (19)

where  $P_{RV,iso}$  is the isovolumic pressure in the RV,  $P_{RV,0}$  is the reference or baseline pressure of the RV, k is a constant proportionality,  $V_{RV,0}$  is the initial volume of the RV and  $V_{RV}$  is the current volume of the RV. k was set to 10000 mmHg ml<sup>-1</sup> to control the pressure needed to maintain a certain volume and was sufficient to obtain the isovolumic phases of the biventricular model. The left and right ventricular pressures for the whole cardiac cycle were governed by the following ODEs in Eq. (20) and (21).

$$P_{LV} = \begin{cases} P_{systemic} + Q_{AV}R_{AV}, & P_{LV,iso} > P_{systemic} \\ P_{LV,iso}, & P_{LV,iso} \le P_{systemic} \\ P_{systemic} \le P_{LV,iso} \end{cases}$$

$$P_{LA} - Q_{mitral}R_{mitral}, & P_{LA} > P_{LV,iso}$$

$$(20)$$

$$P_{RV} = \begin{cases} P_{pulmonary} + Q_{PV}R_{PV}, P_{RV,iso} > P_{pulmonary} \\ P_{RV,iso}, P_{RV,iso} \leq P_{pulmonary} \\ P_{pulmonary} \leq P_{RV,iso} \end{cases}$$

$$P_{RA} - Q_{tricuspid}R_{tricuspid}, P_{RA} > P_{RV,iso}$$

$$(21)$$

404

## 2.6 Coronary flow dynamics

Blood flowing through the coronary arteries was considered to be an incompressible Newtonian fluid with a constant density,  $\rho_f$ =1060 kg/m<sup>3</sup> and dynamic viscosity,  $\mu_f$ =0.00345 Pa.s. Blood flow was assumed to be laminar governed by the Navier-Stokes equation in Eq. (22) and its continuity equation, Eq. (23) ensuring mass conservation within the fluid flow

$$409 \rho_f \frac{\partial u_f}{\partial t} + \rho_f (\vec{u}_f \cdot \nabla) \vec{u}_f = \nabla \cdot [-pI + K] (22)$$

$$410 \rho_f \nabla \cdot \vec{u}_f = 0 (23)$$

411 
$$K = \mu_f \left( \nabla \vec{u}_f + \left( \nabla \vec{u}_f \right)^T \right)$$

where  $\rho_f$  = fluid density,  $\overrightarrow{u_f}$  = fluid velocity vector, p = fluid pressure, and K = viscous stress tensor. For the boundary conditions of the coronary flow model, the aortic inlet was prescribed with the simulated aortic outflow,  $Q_{AV}$  described in Eq. (13) of the Supplementary Materials

I. This coupling ensures that the coronary flow dynamics are driven by the physiologically relevant aortic flow of the simulated biventricular electromechanical model. The aortic outlet was represented with three-element Windkessel model [59, 60] as shown in Figure 3 to simulate the vascular afterload with ODE in Eq. (24) and (25)

$$Q_p = \frac{P_{inlet} - P_p}{R_p} \tag{24}$$

420  $P_p$  is determined from this ODE

421 
$$Q_p = C_p \frac{dP_p}{dt} + \frac{P_p}{R_d}$$
 (25)

where  $Q_p$  is the aortic outflow rate,  $P_{inlet}$  was calculated by averaging the pressure of the aortic outlet boundary,  $R_p = 14.06$  MPa.s/m<sup>3</sup>,  $C_p = 0.001$  cm<sup>5</sup>/dyne and  $R_d = 142.19$  MPa.s/m<sup>3</sup>. The

coronary outlet boundary conditions were set to a constant pressure of 3 mmHg representing the mean right atrial pressure [36, 61]. This simplification serves to approximate the general outflow characteristics without the detailed representation of downstream microcirculatory effects. Ideally, a lumped parameter model for the microcirculation would be applied to better capture the contribution of intramyocardial pressure on coronary flow. However, the focus of this study is to investigate the effect of cardiac motion on coronary flow making the simplification is reasonable.

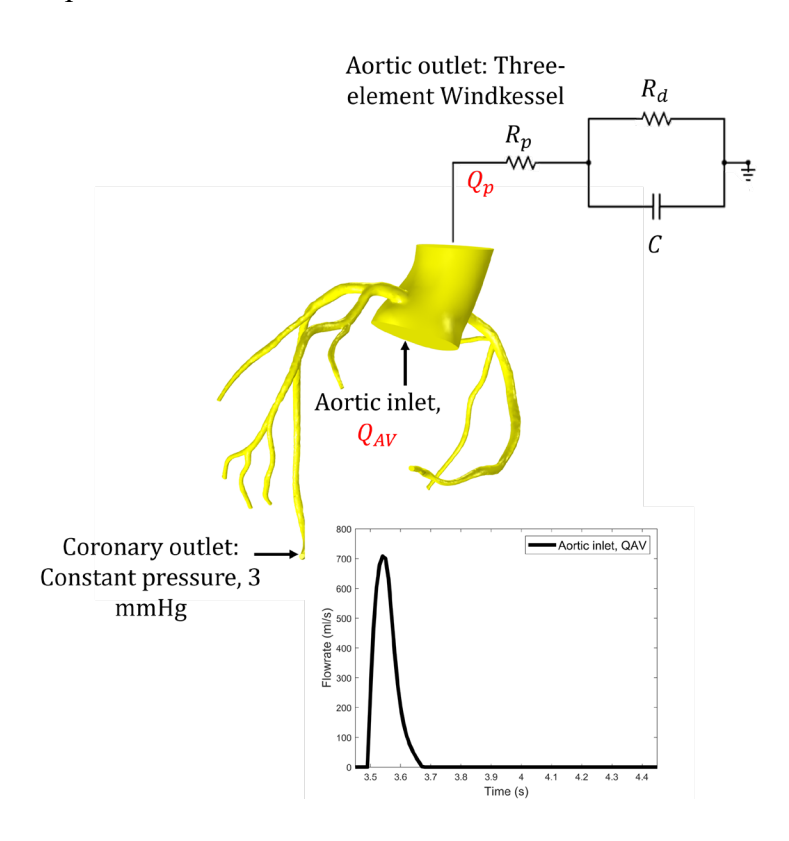


Figure 3 Schematic of the boundary conditions for the coronary artery model. The simulated aortic flow from the electromechanical simulation,  $Q_{AV}$  is prescribed as the coronary aortic inlet condition. The aortic outlet is set with a three-element Windkessel model to represent the systemic flow. Each coronary outlet is governed by a constant pressure of 3 mmHg

## 2.7 Coronary artery-myocardium displacement coupling

To mathematically couple the biventricular electromechanical model with the coronary flow model, we adopted a one-way coupling method which means that the displacement field from the 3D biventricular electromechanics were translated to the coronary arterial walls but the feedback from the coronary arterial stiffness to the myocardium was neglected. We utilized a 'General Extrusion' coupling operator in COMSOL Multiphysics 6.1 (COMSOL AB, Sweden) to map the displacement field from the biventricular domain to the mutual interface

of the coronary artery segment. Using this operator, we specified the biventricular myocardium as a source domain and the coronary artery as a destination domain. An extrusion mapping function was defined to relate the coordinates of the coronary artery segment to those of the myocardium, ensuring accurate transfer of the displacement vector (u, v, w) between the two closest points on the surface of the artery and the epicardial surface of the myocardium. This step ensured that the coronary artery moved through the same displacement field as the nearest position of the epicardium, creating a tethering effect. We did not explicitly model the arterial wall deformation as a separate fluid-structure interaction problem. However, we employed a moving mesh approach in which the coronary arteries were set to follow the myocardial motion. A moving mesh method with Yeoh hyper elastic smoothing method (see Eq. (26)-(28) in Supplementary Materials I) was implemented in the coronary arteries to accurately capture the mechanical interaction and deformation transfer between the myocardium and coronary artery domains similar to previous work [27]. We expect this approach is sufficient considering the artery itself was hyper elastic [62]. An Arbitrary Lagrangian-Eulerian (ALE) formulation was used to handle the deforming domains where the mesh nodes within the myocardium and coronary artery domains were allowed to move according to the prescribed displacement field ensuring accurate propagation of boundary motion. While this does not explicitly capture full arterial wall elasticity and wave propagation effects, it provides a reasonable approximation for investigating the influence of cardiac-induced motion on coronary hemodynamic. The aortic inlet and outlet boundaries were held fixed in space.

463

464

465

466

467

468

469

470

471

472

473

474

443

444

445

446

447

448

449

450

451

452

453

454

455

456

457

458

459

460

461

462

## 2.8 Numerical setup

A mesh independence study was conducted using COMSOL's default mesh settings: Coarse, Normal, Fine and Finer. In this study, the mesh convergence for the fluid dynamics of the coronary arteries was assessed. The value of maximum coronary flow at peak systole was selected as the comparison metric to determine the optimal mesh configuration (see **Table 2** and **Figure 3** in **Supplementary Materials I**). The fine mesh was selected as the optimal configuration, as the peak systolic coronary flow values deviated by less than 10 % compared to those obtained with the finer mesh. The coronary artery mesh was mostly comprised of tetrahedral elements followed by a smaller proportion of pyramidal, prismatic, triangular and quadrilateral elements. Tetrahedral elements were predominantly used for volume meshing due to their flexibility in capturing complex arterial geometries. Pyramidal and prismatic elements

were incorporated in boundary layers to enhance accuracy in resolving near-wall flow gradients. Additionally, triangular and quadrilateral elements were employed in surface meshing to maintain smooth transitions and improve numerical stability.

475

476

477

478

479

480

481

482

483

484

485

486

487

488

489

490

491

492

493

494

495

496

497

498

499

500

501

502

503

504

505

506

507

We first conducted a standalone biventricular electromechanical simulation to obtain essential data including the aortic flow rate, as well as the left and right ventricular pressures. The output from this simulation was then used to drive the simulation of the coronary artery flow model. We employed a weakly coupled approach rather than solving all physics simultaneously reducing the complexity and computational time. The simulation began with a stationary solver to resolve the myocardial fibre mechanics. This was followed by a timedependent solver to solve the electrophysiology and active stress equations, with electrical stimulus first applied to the biventricular apical region at t=0.45 seconds. The simulation was conducted over a total duration of 1 second, corresponding to a single cardiac cycle at a heart rate of 60 beats per minute. Then, the biventricular motion was solved under a quasistatic assumption by implementing the previously computed active stress in the equation of motion. For the solid mechanics physics in this simulation, the finite element discretization was set to use the COMSOL's default setting of 'quadratic serendipity' elements for the displacement field. These elements offer fewer nodes per element compared to 'quadratic Lagrange' elements, offering a good balance between accuracy and computational efficiency. After running the electromechanical simulation, the laminar flow simulation for the coronary circulation model was performed. For solving the laminar flow, the discretization was set to use P1 + P1 elements, which is the default element order for laminar flow governed by the Navier-Stokes equations in COMSOL. The abbreviation P<sub>m</sub>P<sub>n</sub> refers to the polynomial order of the shape functions (elements) for the velocity components (m) and pressure (n) when employing tetrahedral or triangular elements. The P1 + P1 elements choice employs linear elements for both the velocity components and pressure fields and were selected to ensure computational efficiency while maintaining acceptable accuracy, given the computational demands of the multiphysics simulation in this study. The simulation was run for four cardiac cycles to ensure the formation of stable cycles. A fully coupled Parallel Direct Solver (PARDISO) with an automatically damped Newton method was employed for all formulations. A fifth-order implicit Backward Differentiation Formulation (BDF) solver was used to update the variables at each time step with results recorded every 2 milliseconds. We utilized the Iridis 5 high-performance computing (HPC) cluster facilitated by University of Southampton, specifically leveraging one Intel compute node for computation. Each Intel node in Iridis 5 is equipped with dual 2.0 GHz Intel Xeon Gold 6138 processors, providing a total of 40 CPU cores per node that have 192 GB of DDR4 memory. The breakdown of the substantial computational resources in simulating the framework model of the cardiac electromechanics – coronary flow is presented in **Table 3** in **Supplementary Materials I**. Overall, the total computation time to simulate a full cardiac cycle, including both myocardial electromechanics and coronary flow was approximately 14 hours and 30 minutes. The primary factors influencing the computational efficiency include the complexity of the multiphysics coupling that required for solving large nonlinear systems in myocardial mechanics and capturing the interactions between electromechanics and coronary flow dynamics.

#### 3.0 Results and discussion

519

520

521

522

523

524

525

526

527

528

529

530

531

532

533

534

535

536

537

538

539

540

541

542

543

544

545

In this study, results are presented from the last cardiac cycle of the simulation timeframe specifically spanning from t=3.45 seconds until t=4.45 seconds (stimulus was activated at t=3.45 seconds) to provide a stable representation of the data for analysis.

## 3.1 Electromechanical

The spatial distribution of membrane potential,  $V_m$ , active stress,  $T_a$  and recovery, R phases across the biventricular model at certain time points throughout the cardiac cycle are depicted in Figure 4 (A-C) and the curve profiles are shown in Figure 4 (D-F). Based on Figure 4 (A), the electrical activation is initiated at the apical region (bottom part of the heart) of the biventricular model. The action potential propagates through the ventricles and fully activates them within 100 milliseconds. In healthy humans, the total ventricular depolarization lasts approximately 70 - 110 milliseconds [63]. The membrane potential waveform in Figure 4 (D) indicates a rise in voltage instantly following the stimulation, peaking at 20 mV during the depolarization phase. It then gradually repolarizes and returns to the resting membrane potential of -80 mV. The action potential duration is approximately 250 milliseconds, aligning with the physiological range for humans, typically between 200 and 400 milliseconds [63, 64]. The active stress distribution as seen in Figure 4 (B) shows that the maximum stress occurs at the apical region once they are fully electrically activated at t=3.55 seconds and spread through the biventricular model to bring the mechanical contraction (systole). The active stress waveform in Figure 4 (E) proves that the biventricular myocardium peaks shortly after depolarization, preparing the ventricles to contract. It shows a rapid increase followed by a linear decline, reaching a peak stress of 224 kPa. The following recovery phase (diastole) begins at t=3.65 seconds and peaks at t=3.75 seconds at the basal region (top part of the heart) as seen in Figure 4 (C). The recovery plot in Figure 4 (F) demonstrates that after the action potential,  $V_m$  is generated, R gradually increases. As R increases,  $V_m$  gradually repolarizes before declining as R reaches its maximum. Once the membrane potential returns to the resting state, R decreases sharply.

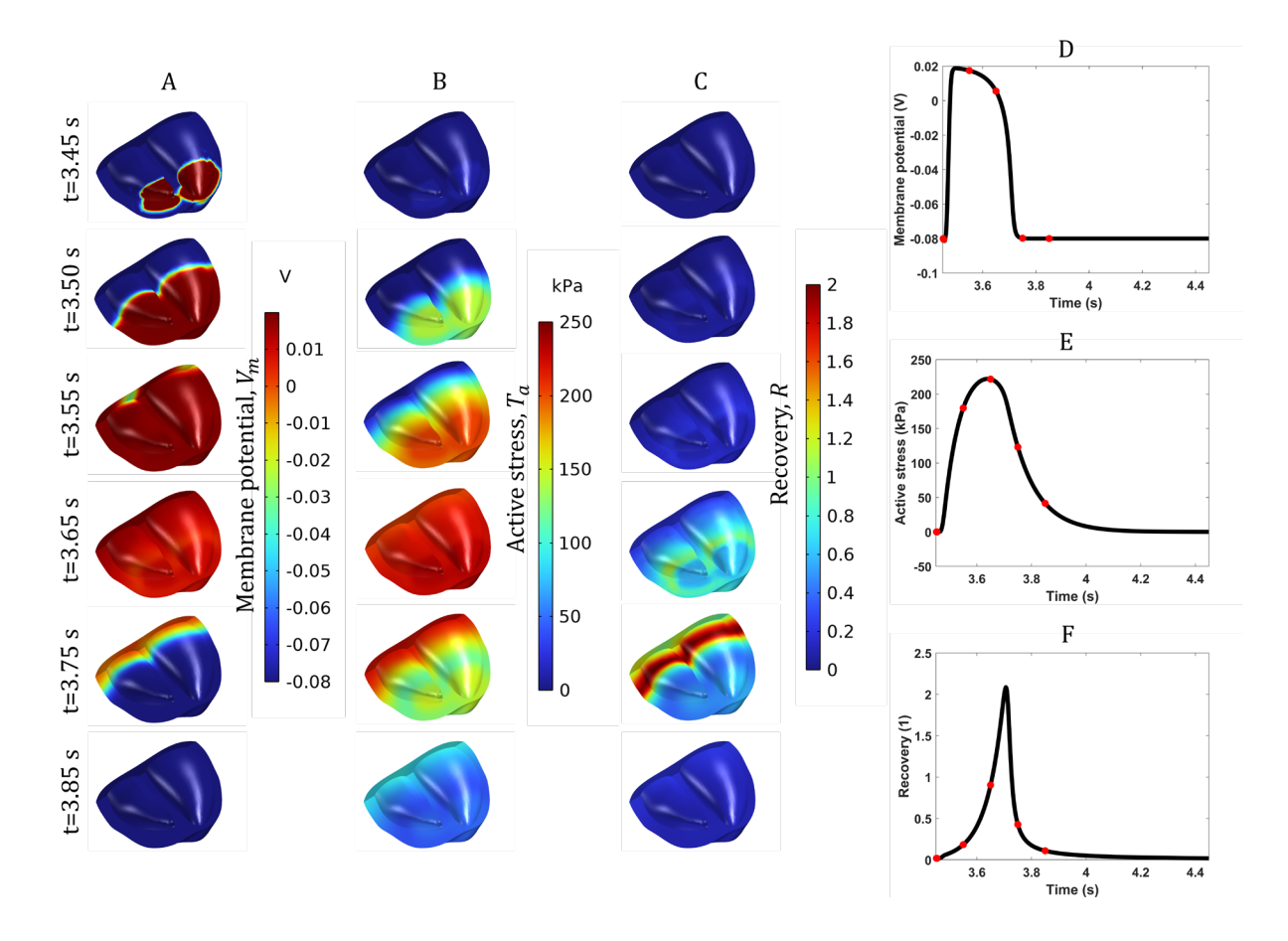


Figure 4 Snapshot distribution of the (A) membrane potential (B) active stress and (C) recovery phases of the simulated biventricular electromechanics at various time points (Stimulus was activated at t=3.45 seconds). (D-F) show the waveform profiles of  $V_m$ ,  $T_a$  and R, respectively. The markers in the plot show the time points where data was obtained

## 3.2 Pressure and volume

To assess the contractility of the biventricular model, we obtained the pressure and volume changes in the ventricles over a cardiac cycle. Figure 5 (A) and (B) present the pressure and volume waveforms of the LV and RV over a complete cardiac cycle. The LV and RV pressures rise rapidly during systole reaching maximum values of 126 mmHg and 30 mmHg, respectively. The pressures then gradually drop until reaching minimum values of 16 mmHg and 7 mmHg. Figure 5 (C) presents the pressure-volume loops of the left and right ventricles. It illustrates that during the ventricular filling phase, the chambers expand to reach its maximum volume. The end-diastolic volume (EDV) are 118 ml and 89 ml, each for LV and RV. As systole begins, the ventricles contract with the volume remains constant for a short time (isovolumic contraction). This is followed by the ejection phase where the volume decreases rapidly to the end-systolic volume (ESV), with the LV and RV reaching ESV of 59 ml and 42

ml, respectively. After ejection, the ventricles relax during a period of constant volume (isovolumic relaxation) before the filling resumes and the volume increases again. The computed stroke volumes of the LV and RV are 59 ml and 47 ml, respectively with ejection fractions (EF) of 50 % and 53 %, respectively. The EF of the LV is slightly below the normal range of 52% to 74 % [65], likely due to under-segmentation of the biventricular chamber during pre-processing. The upper biventricular segment was removed, and the lower part was held fixed without motion, resulting in reduced chamber volume and potentially limiting maximal contraction thus generating a lesser cardiac output. **Figure 5 (D)** shows the pressure waveforms of the LV and aorta where the aortic pressure curve reflects the ejection phase with pressure ranges between 79 mmHg and 87 mmHg during systole.

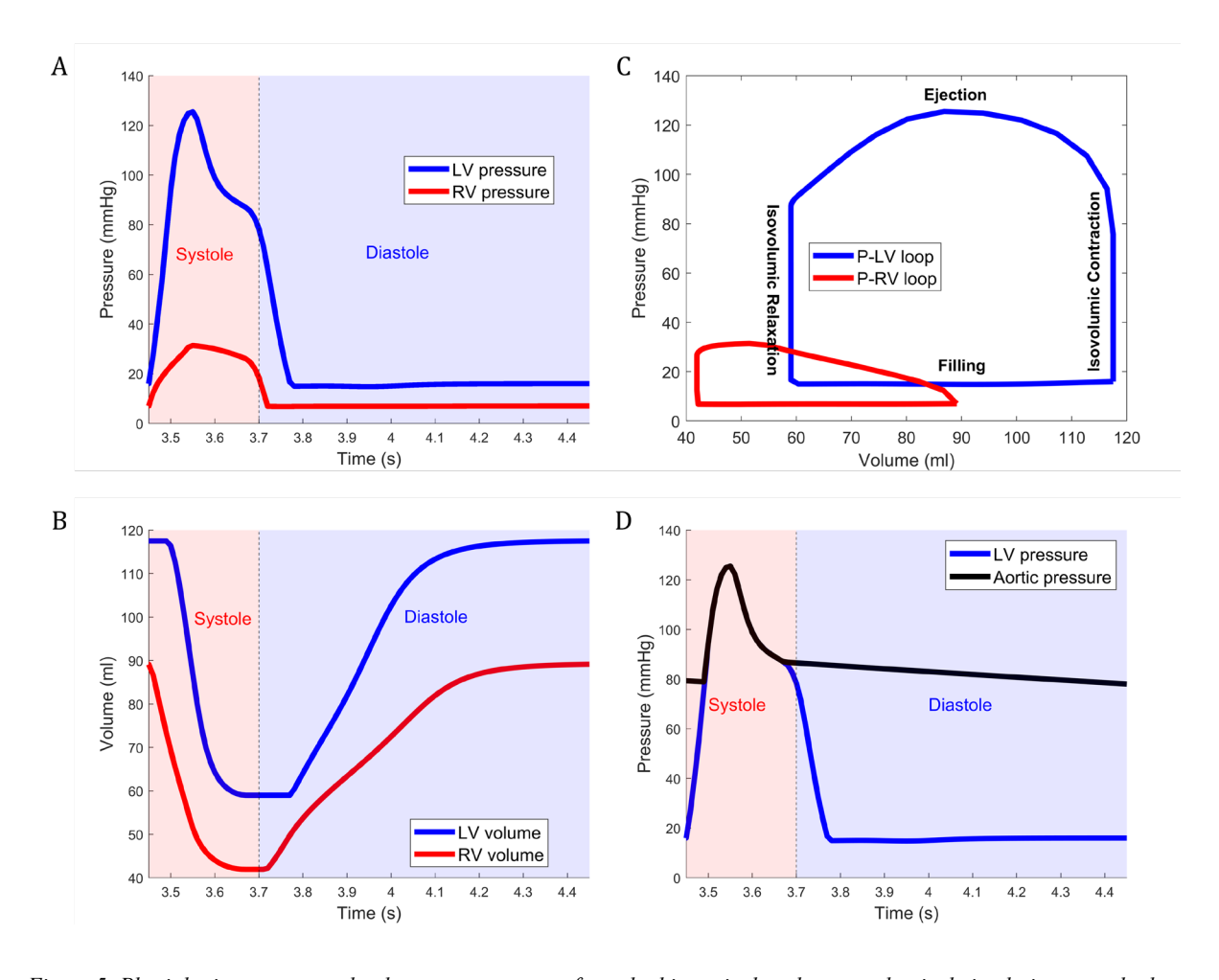


Figure 5 Physiologic pressure and volume measurements from the biventricular electromechanical simulation over the last cardiac cycle (Stimulus was activated at t=3.45 seconds). (A) LV and RV pressure traces during systole and diastole. (B) Volume changes of the LV and RV chambers. (C) Pressure-volume loops highlighting the EDV and ESV, to show the biventricular contractility performance. (D) LV and aortic pressure profiles, showing the relationship between the ventricular and systemic pressures

## 3.3 Myocardial – coronary displacement

For brevity, results from the analysis of three coronary arteries LAD2, LCX3 and RCA2 are reported. Figure 6 (A) displays the 3D displacement magnitudes of the biventricular model throughout the cardiac cycle. With the myocardial base fixed, the apex exhibits significant mechanical motion primarily upward displacement toward the fixed base which serves as the reference point. During ventricular systole, the myocardium deforms with the apex displaced by a maximum of 2 cm from its original position. During diastole, the myocardium returns to its initial configuration enabling biventricular filling. Figure 6 (B) illustrates that the displacement magnitude at one corresponding point on the shared boundary between the myocardium and the closest point of the LAD2, LCX3 and RCA2 are identical. This confirms that the coupling operator effectively maps the displacement from the myocardium to the coronary arteries. The precise alignment of displacements ensures similar mechanical deformations in the coronary arteries, validating the robustness of the coupling method used. The findings also show that the LAD2 artery undergoes the greatest displacement of 1 cm as it is located at the apex which experiences the greatest motion.

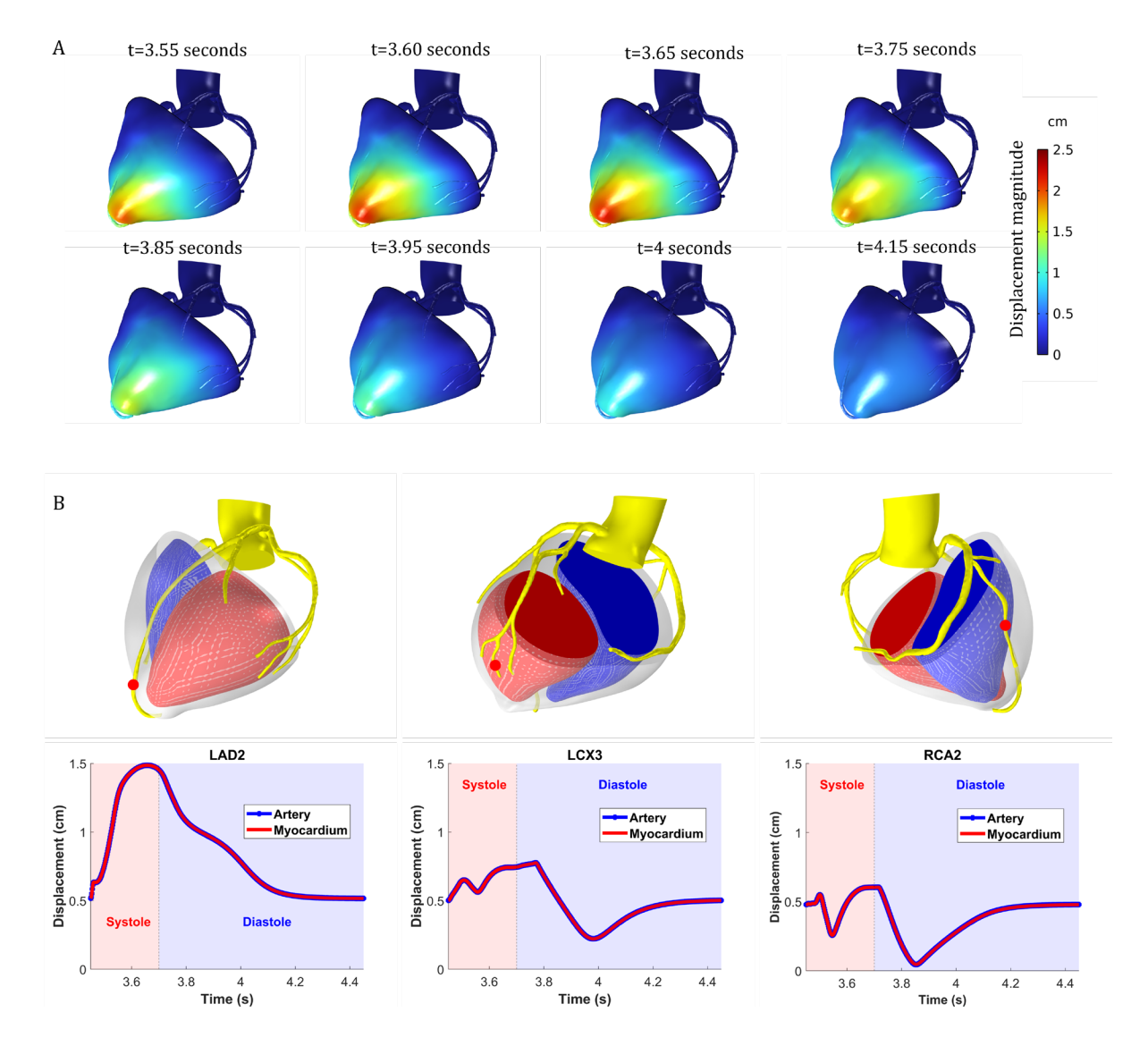


Figure 6 Myocardial-coronary artery displacement at selected time points throughout a cardiac cycle (Stimulus was activated at t=3.45 seconds). (A) The distribution of displacement magnitude across the electromechanical coupling model showing significant displacement of the apex during systole compared to the base, which remains fixed. During diastole, the model returns to its original position. (B) The displacement magnitude recorded at a point on the shared myocardial boundary and the corresponding closest point in the LAD2, LCX3 and RCA2 segments. The synchronized waveform indicates the successful mathematical coupling between the myocardium and coronary arteries achieved using the general extrusion coupling operator

# 3.4 Pressure, velocity and flow profiles of the coronary arteries

Local pressure, velocity and flow profiles were analysed from our two case models: the moving and non-moving coronary artery models to assess the variability of the coronary haemodynamic with and without cardiac-induced motion. **Figure 7 (A-C)** displays the profiles of local pressure in the LAD2, LCX3 and RCA2 segments, respectively. Our findings show that the moving coronary arteries model has higher pressure distribution than the non-moving

arteries model. The moving LAD2 in Figure 7 (A) produces a peak systolic pressure of 83 mmHg, compared to 76 mmHg in the non-moving LAD2. Similarly, Figure 7 (B) shows that the moving LCX3 reaches a maximum systolic pressure of 42 mmHg while in the non-moving model this was 16 mmHg. For RCA2, as depicted in Figure 7 (C), the moving model has a peak pressure of 68 mmHg, whereas in the non-moving model this was 57 mmHg. The LAD2 is located at the apex of the biventricular model which experiences more pronounced motion compared to other ventricular regions and having larger compressive forces than the LCX3 and RCA2. The LCX3 and RCA2 are situated near the myocardial basal region, which is less influenced by the myocardial motion, resulting in comparatively lower pressures. In addition to the pressure variations, Figure 7 (D-F) present the local velocity profiles to provide further insights into the flow dynamics. Our results show that the local velocity profiles of the nonmoving coronary arteries model are greater than the moving coronary arteries model. It is shown in Figure 7 (D) that the non-moving LAD2 has a slightly higher peak velocity of 1.8 m/s and 1.4 m/s for the moving LAD2. Based on Figure 7 (E), the non-moving LCX3 has a maximum velocity of 2.3 m/s while the moving LCX3 shows a lower value of 1.6 m/s. Correspondingly, the non-moving and moving model of RCA2 has a maximum velocity of 1.8 m/s and 1.4 m/s respectively as shown in Figure 7 (F). The flow profiles of the coronary arteries are shown in Figure 7 (G-H). Based on the flow profiles of the LAD2 in Figure 7 (G), the peak systolic flow rate are 6.6 ml/s and 3.7 ml/s for the non-moving and non-moving model, respectively. For the LCX3 in Figure 7 (H), the non-moving model has the maximum systolic flow rate of 2.5 ml/s and 1.8 ml/s for the moving model. Similarly, the non-moving model of RCA2 has higher flow rate during systole of 4.5 ml/s while the moving RCA2 is 3.6 ml/s.

610

611

612

613

614

615

616

617

618

619

620

621

622

623

624

625

626

627

628

629

630

631

632

633

634

635

636

637

638

639

640

641

Since the coronary arteries are embedded on the myocardial tissue, they undergo complicated movement and deformation during cardiac cycle induced by the myocardial mechanics. In our study, the moving coronary artery model is believed to undergo changes in the arterial curvature especially during systole that may contribute to the little driving pressure in the arterial segment compared to the non-moving artery model. The moving arteries could add inertial force [66] to the blood flow that contribute to flow acceleration and elevate local pressure temporarily. Consequently, change in the local arterial shape may change the local arterial resistance, resulting with increased local pressure and reduced local velocity. In the case of the non-moving model, the dynamic effects are absent as the arteries encounter no motion thus producing smoother forward flow with higher velocities and less pressure losses.

In our case models, the coronary flow profiles are as expected to follow the aortic and coronary arterial pressure waveforms which the flow peaked during ventricular systole rather than exhibiting the physiological phasic flow patterns [67-69]. This is primarily due to the absence of intramyocardial pressure effect in the present study, which can be achieved if a lumped parameter model was adopted to simulate the increased flow resistance in coronary microcirculation. Physiologic phasic pattern is associated with the left coronary artery which is characterized by reduced flow during systole and dominant diastolic flow, as a consequence of compressive effects of intramyocardial pressure [70-72] on the intramural vessels. Instead, a constant pressure of 3 mmHg was applied at the coronary outlets of our model instead [36], representing the venous pressure for simplicity, as we were aiming to observe the effects of coronary motion. For comparison of blood flow in the moving and non-moving coronary arteries, the flow rates in moving arteries are lower due to the dynamic changes in arterial shape throughout the cardiac cycle. These arteries experienced non-uniform flow distribution that lowers the overall flow rate compared to the non-moving arteries where flow distribution is uniform.

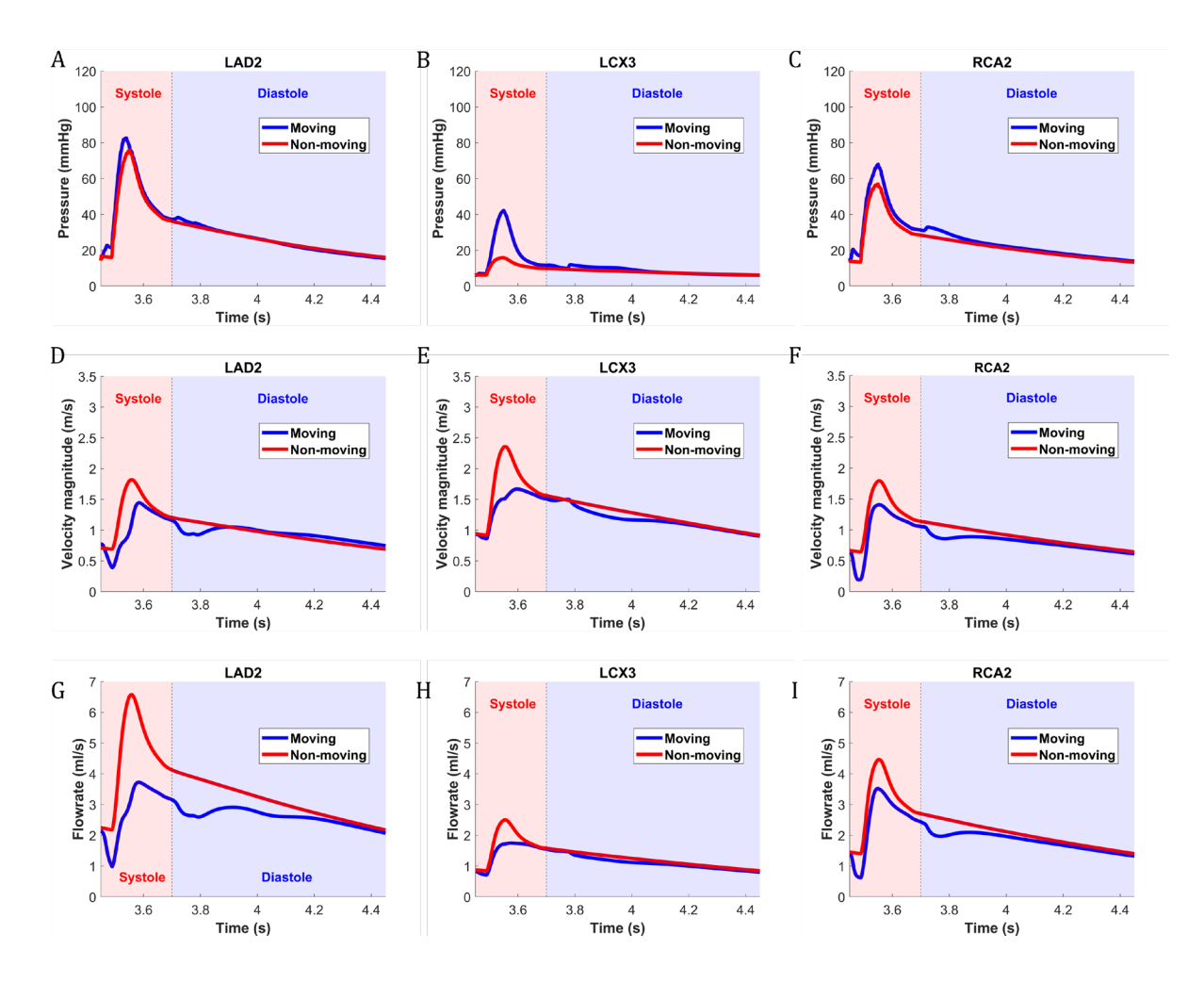


Figure 7 Comparison of local haemodynamic parameters of the moving and non-moving coronary arteries models throughout the cardiac cycle (Stimulus was activated at t=3.45 seconds). (A-C) Local pressure at specific points within the LAD2, LCX3 and RCA2 segments. (D-F) Local velocity at corresponding points in the LAD2, LCX3 and RCA2 segments. (G-I) Flowrate through the LAD2, LCX3 and RCA2

## 3.5 Secondary flow pattern

Blood flow patterns in coronary arteries are of clinical interest due to the potential involvement in the localization of atherosclerosis and CAD. Arterial curvature and its variation during the cardiac cycle can lead to flow irregularities, such as an altered Dean flow characteristics and oscillating wall shear stress [73, 74]. **Figure 8** shows the cross-sections of velocity magnitude of the LAD2, LCX3 and RCA2 that shows the velocity contours formed in the arteries. **Panels (A-F)** present the results for the moving arteries model, while panels (**G-L**) correspond to the non-moving arteries model, both evaluated at peak systole (t=3.55 seconds) and peak diastole (t=3.77 seconds). Consistent with the quantitative velocity profiles shown in **Figure 7**, the velocity contours for both the moving and non-moving models

illustrates the blood velocity magnitude is elevated in the coronary arteries during systole than during diastole, as blood is pumped out of the LV into the arteries. Comparing the pattern of the contours between the moving and non-moving models, the moving arteries (see Figure 8 (A-C)) undergo strong disturbances that cause the primary flow to skew toward the arterial outer wall, resulting in a contour pattern that with higher velocity near that wall. During diastole (see Figure 8 (D-F)), when the arteries are relaxed, the velocity contours exhibit a uniform flow distribution, indicting a full, unskewed primary flow through the coronary arteries. The similar characteristics of velocity contours are shown in the non-moving arteries model both during systole (see Figure 8 (E-H)) and diastole (see Figure 8 (I-K)).

Throughout the cardiac cycle, the motion of the coronary arteries induced by cardiac contraction leads to changes in arterial shape, which likely cause dynamic changes in arterial curvature, introducing additional force to the flow, causing the flow to skew toward the arterial outer wall. As a result, it creates a region with higher velocity near the wall, creating non-uniform velocity field profile. This is reflected in the velocity contours which distribution of low and high velocities across the cross-section of the artery. During diastole, however, the coronary arteries are more relaxed and less affected by the compressive force from the contraction, although the still experienced some effects of the myocardial motion. The flow is more evenly distributed resulting in a relatively uniform velocity contour profile.



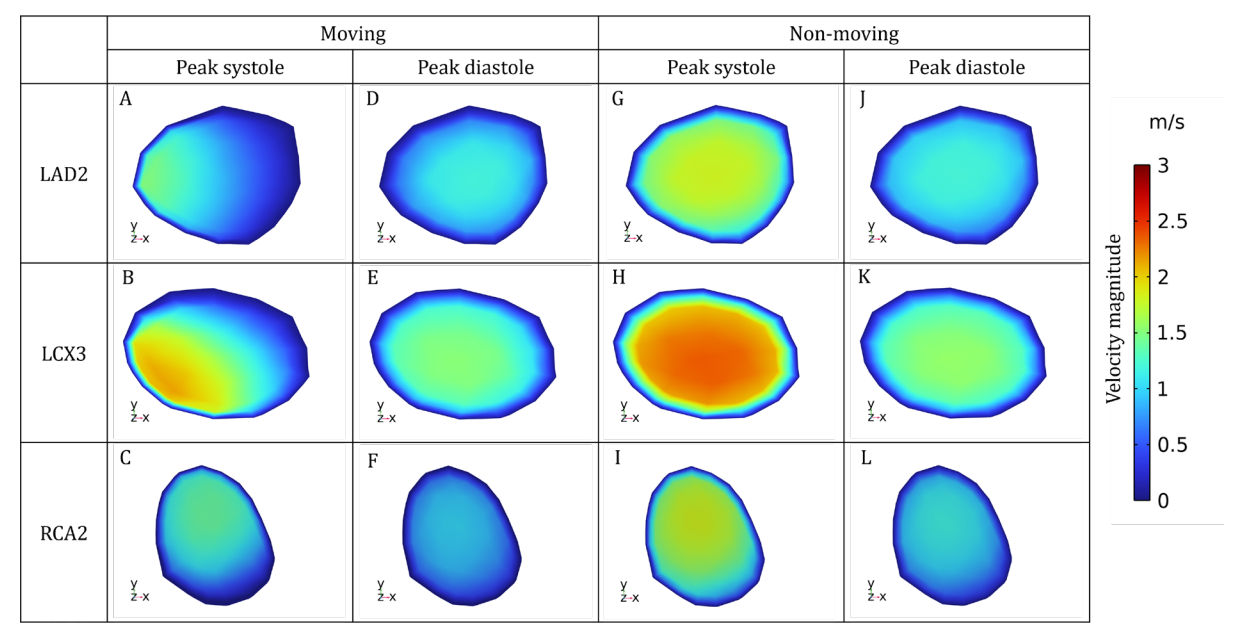


Figure 8 Comparison of velocity magnitude contours at peak systole and peak diastole in the moving and non-moving model of LAD2, LCX3, and RCA2 cross-sectional planes

Next, we obtained the graphical streamlines of secondary in-plane flow pattern of the LAD2, LCX3 and RCA2 to observe the characteristics of the secondary flow under the influence of arterial motion. In Figure 9 (A-C), we can see that the moving arteries, specifically the LCX3 and RCA2 show the presence of single elongated vortex structure, creating a unique secondary flow pattern. Nevertheless, during diastole (see Figure 9 (D-F)), there are no appearance of the secondary vortices in the moving arteries as the blood flows in an orderly manner at lower velocity values compared to systole. In contrast, the non-moving arteries at the peak systole (see Figure 9 (G-I)) and diastole (see Figure 9 (J-L)), exhibit prominent secondary flow patterns with dual vortices structures are produced in the LCX3 and RCA2. In the LCX3, two counter-rotating Dean-like vortices are visible whereas in the RCA2, the size of the dual vortices are distorted, with one of the vortices tend to be elongated. Compared to the LCX3 and RCA2, the LAD2 exhibits distinct characteristics in its velocity profiles, which appear less prominent in the visual representation. This difference may stem from the anatomical positioning of the LAD2 in our segmented model as major of its segments are predominantly embedded within the myocardium. The LCX3 and RCA2 in contradict, are

largely situated on the myocardial surface. Therefore, this structural distinction likely influences the flow dynamics as observed in the LAD2.

709

710

711

712

713

714

715

716

717

718

719

720

721

722

723

724

725

726

727

728

729

730

731

Blood flow in coronary arteries is mostly laminar and may generate secondary flow due to vessel curvature or bifurcation [73, 75]. High-velocity flow in curved arteries causes the blood flow to skew toward the arterial wall (swirling effect), creating centrifugal forces. These forces create a secondary flow perpendicular to the primary flow direction, leading to the formation of counter-rotating Dean vortices. Our findings show that the Dean-like vortices clearly appear in the non-moving coronary arteries due to the steady flow profiles where the centrifugal forces dominate over the transient inertia effects [76]. Regarding the asymmetry structure of the counter-rotating Dean vortices, these studies [73, 77-79] reported similar findings in their analysis of helical pipes and coronary artery in different range of torsion or curvature, that an increase in the torsion causes a twisting effect on the interface between the two vortices which leads to the expansion of one of the vortices. On the other side, Dean-like vortices in the moving artery model appears to be washed out and less pronounced as seen in this work [69]. Similarly, this work [77] showed that the symmetric structures of their counterrotating vortical cells of a baseline graft model are distorted by the helix and nonplanar flow paths introduced in their grafts model. They also found that the degree of the asymmetry increases downstream as swirling intensity of the flow in the graft increases. In our case, the moving coronary arteries induced by cardiac motion throughout the cardiac cycle causes the flow to be exceptionally dynamic and chaotic therefore the vortices are less stable and disrupted. Such changes likely will affect transport characteristics, such as nutrient transport and lipid deposition, thus possibly promoting atheroprotective effect, however, further study is warranted.

	Mov	ving	Non-moving	
	Peak systole	Peak diastole	Peak systole	Peak diastole
LAD2	A	D	G	J
LCX3	B	E	H	K
RCA2	C	F	I	L

Figure 9 Comparison of secondary in-plane flow streamlines on the cross-sections of the moving and non-moving LAD2, LCX3, and RCA2 to evaluate the impact of motion on the flow characteristics. Note that the streamlines represent the general graphical pattern of secondary flow, not primary flow

# 3.6 Wall shear stress and time-averaged wall shear stress

The instantaneous WSS profiles of the LAD2, LCX3 and RCA2 at peak systolic and peak diastolic are compared to examine the effects of coronary arterial motion on the instantaneous haemodynamic as shown in **Figure 10**. It is clearly shown that the moving coronary arteries produce higher WSS than the non-moving coronary arteries model near the bifurcation region and distal end of the arteries. **Table 5** presents the maximum WSS values for the LAD2, LCX3 and RCA2 arteries during peak systole and diastole. In the moving model, the LAD2 at peak systole creates a region with a higher WSS with a maximum value of 22.7 Pa than the peak diastole with maximum value of 15.3 Pa. The non-moving LAD2 at peak systole has a maximum WSS of 22.2 Pa and 13.5 Pa during peak diastole, very slightly lower value than the moving model. The LCX3 demonstrates the highest WSS in the moving model, reaching 42.3 Pa during peak systole and 24.6 Pa during the peak diastole, whereas the non-moving LCX3 show notably lower WSS values of 28.3 Pa and 17.6 Pa, respectively. A similar pattern is observed for the RCA2, where the moving model of RCA2 depicts greater WSS values compared to the non-moving model.

Our findings reveal that dynamic motion of the coronary arteries induced by cardiac movement leads to higher WSS values might drive by the inertial effect and changing of the arterial curvature throughout the cardiac cycle. The significant impact of coronary arterial motion on instantaneous WSS on these reports [20, 21] further supports this observation. Consequently, the dynamic motion of the coronary arteries may confer an atheroprotective effect, as regions with low WSS are known to promote atherosclerosis. However, this review [80] suggested that both low and high wall shear stress in arteries have been associated with plaque development and vulnerability as shown by clinical imaging studies and the exact nature of these relationships remains poorly defined and sometimes inconsistent across studies. Therefore, as coronary artery motion influences the WSS distribution, this analysis highlights the importance of accounting arterial motion when studying coronary biomechanics. Neglecting it in computational models may underestimating the biomechanical factors driving CAD progression.

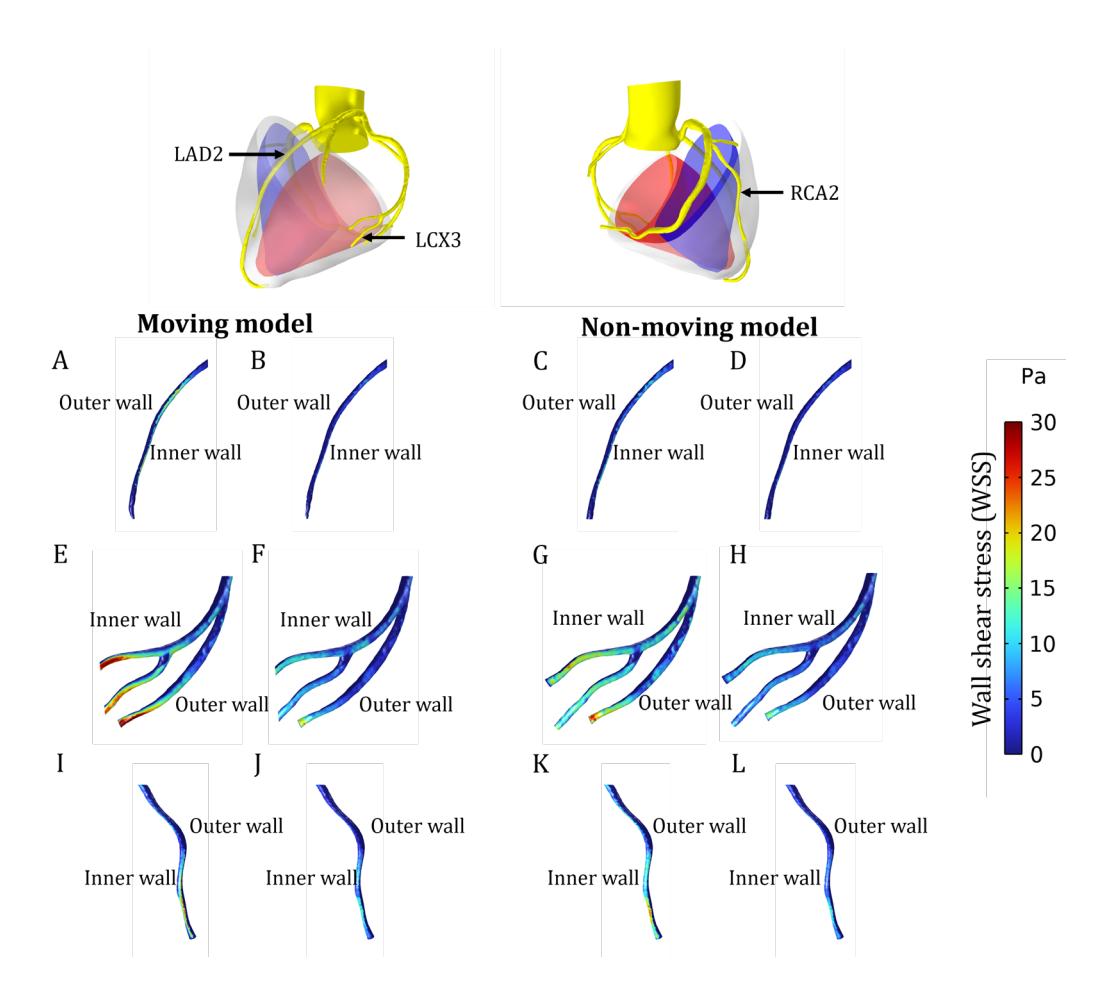


Figure 10Wall shear stress (WSS) distribution in the LAD2, LCX3 and RCA2 during peak systolic and diastolic phases to compare the variations between moving and non-moving arterial models. (A,B) show the WSS field of the moving LAD2 during peak systole and diastole, respectively with higher WSS observed in (A). (C,D) depict the WSS field of the non-moving LAD2, showing slightly higher WSS in (C). (E,F) illustrate the WSS field of the moving LCX3 with (E) exhibiting the highest WSS at

the distal end of the artery. (G,H) present the WSS field of the non-moving LCX3, where (G) produces greater WSS than (H).

(I,J) display the WSS field of the moving RCA2 highlighting greater WSS in (I). (K,L) show the WSS field of the non-moving

RCA2, with (K) exhibiting greater WSS than (L)

Table 5 Maximum wall shear stress (WSS) at peak systolic (t=3.55 seconds) and peak diastolic (t=3.70 seconds) for the moving and non-moving arteries LAD2, LCX3 and RCA2

ſ		Moving model		Non-moving model	
	Arteries	Maximum WSS at peak systole (Pa)	Maximum WSS at peak diastole (Pa)	Maximum WSS at peak systole (Pa)	Maximum WSS at peak diastole (Pa)
I	LAD2	22.7	15.3	22.2	13.5
I	LCX3	42.3	24.6	28.3	17.6
ſ	RCA2	29.7	17.0	27.5	15.3

The comparison of the time-averaged WSS (TAWSS) between the moving and non-moving coronary artery models in our study revealed that the difference in TAWSS distributions is generally insignificant as shown in **Figure 11**. Based on the TAWSS field across the arterial segments, it demonstrates that region with high and low WSS are consistent across both models. This suggests that the inclusion of coronary arterial motion has limited impact on the overall spatial pattern of TAWSS in coronary arteries. These findings align with prior studies investigating the effects of cardiac motion on coronary artery haemodynamic. For instance, Zeng et al. [20] observed that while cardiac motion varies the instantaneous WSS notably, the TAWSS however were similar between the dynamic and static models. Similarly, Torii et al. [21] reported that the TAWSS for the case without the dynamic vessel motion shows a similar pattern with the case with dynamic vessel motion. They concluded that the dynamic motion primarily modulates the instantaneous flow feature of WSS while remain relatively stable for the TAWSS. The variations in the coronary arterial curvature may influence the short-term WSS however these effects tend to average out over the entire cardiac cycle.

## Moving model Non-moving model

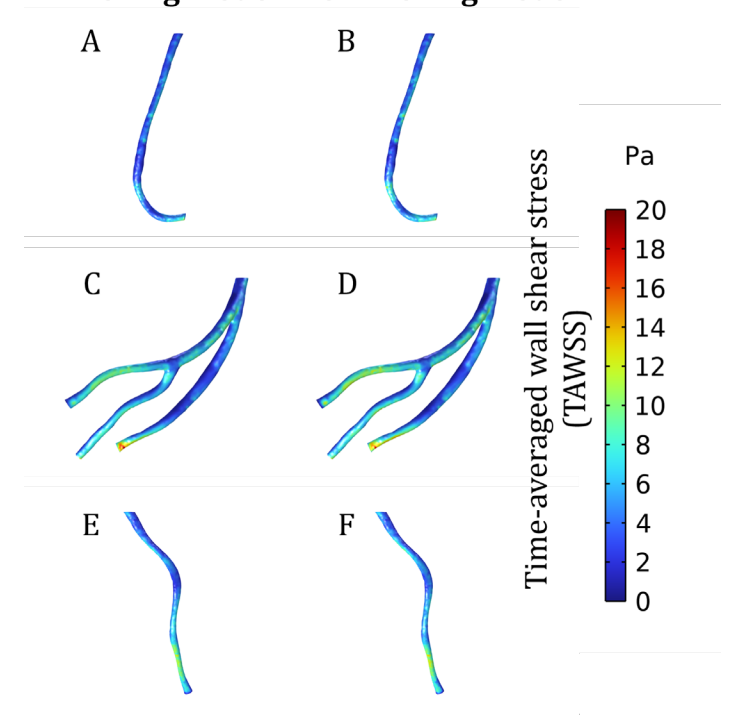


Figure 11 Comparison of the time-averaged wall shear stress (TAWSS) in the moving and non-moving LAD2, LCX3 and RCA2 throughout a cardiac cycle. (A) the moving LAD2 (B) the non-moving LAD2 (C) the moving LCX3 (D) the non-moving LCX3 (E) the moving RCA2 (F) the non-moving RCA2

## 4.0 Limitations

There are several limitations associated with this study. First, the patient-specific model considers the biventricular myocardium but excludes physical representation of the atrial chambers. While atrial contraction contributes to the ventricular blood filling, incorporating atrial dynamics would require additional computational costs and for studies focusing primarily on coronary flow and ventricular mechanics, the direct contribution of active atrial dynamics may alter the diastole myocardial strain but likely have a relatively smaller impact compared to the early passive filling phase. Second, the upper portion of the biventricular model is truncated enabling a high-quality mesh to be constructed in the relatively smooth geometry. While removing the atria and some parts of the upper right myocardial regions, this has led to an under segmentation of the RV leading to a reduction in RV stroke volume. Furthermore, we assumed the myocardial base as our fixed point of reference similar to [25], which may overconstraint the basal displacement. In reality, the heart's apex is fixed in place in actual physiology, which can alter the systolic behaviour [74]. This selection of fixed point of

reference was due to simplicity in achieving faster convergence. However, it might cause slight deviations in the simulated pressure and volume from normal physiological ranges. Third, the cardiac circulatory system is modelled using an open-loop configuration. A closed loop circulatory model would provide more realistic feedback on pressures and flows from the interaction between the systemic circulation and the heart, which can also guarantee an equal stroke volume, but this would add considerable complexity as it requires additional parameter such as venous return and requires more cycles to achieve stable cardiac cycle. Fourth, the coronary outlet boundary condition was set with a constant pressure that provides a straightforward way to model the flow which we also neglected the coronary microcirculation, focusing only on the flow in the large epicardial coronary arteries. Since the primary goal was to investigate the effect of cardiac-induced coronary arterial motion on coronary flow, modelling the downstream microcirculation will be considered in future work when investigating downstream perfusion. Nevertheless, each limitation is a deliberate trade-off to meet the study's main objective without overburdening the framework model.

## 5.0 Conclusion

In this paper, we presented a framework model that couples a 3D biventricular cardiac electromechanics model with a 3D coronary artery flow model to investigate the significance of cardiac induced-coronary arterial motion on coronary haemodynamic. There are two key contributions in this study. First, we introduced a simplified one-way coupling approach to integrate a comprehensive biventricular electromechanical model - encompassing mathematical formulations for fibre orientation, electrophysiology, anisotropic ventricular properties and mechanics with a coronary flow model via data mapping. To address the computational expense and potential of solving complex multiphysics problems in a single framework, we adopted a segregated approach solving the cardiac electromechanics and coronary flow models as separate components. Nevertheless, we ensured consistent displacement between the biventricular myocardium and coronary arteries through mathematical data mapping. Second, we show the significance of incorporating cardiacinduced coronary arterial motion in simulating cardiac electromechanics-coronary flow model. The complex motion of coronary arteries alters the arterial shape i.e. curvature which impacts the pressure, velocity and flow profiles. We demonstrated that the cardiac-induced motion in curved arterial geometries generates unique secondary flow patterns throughout the cardiac

cycle, modifying the structure of Dean-like vortices. The dynamic artery model tends to wash out the Dean vortices. Furthermore, the arterial motion notably affects the WSS profiles, potentially influencing the initiation and progression of atherosclerosis. These findings suggest that accounting for physiological cardiac motion when quantifying coronary blood flow can bring divergent conclusions for the coronary haemodynamic metrices, which can be essential for the prediction of CAD in patients. Overall, this comprehensive framework offers a simplified yet robust approach to simulate physiological and pathological heart conditions for personalized medicine, enabling the study of myocardium-coronary vessel interactions and coronary artery diseases which can significantly impact patients' heart health.

## **Declaration of Competing Interest**

The authors declare that they have no conflict of interest.

## Acknowledgements

This project has received funding from the Fundamental Research Grant Scheme (FRGS/1/2020/TK0/USMC/02/5) under the auspices of the Malaysian Ministry of Higher Education (MoHE). The authors would like to acknowledge the use of the Iridis 5 HPC facility at the University of Southampton.

## Declaration of generative AI and AI-assisted technologies in the writing process

During the preparation of this work the author(s) used generative AI for writing purposes for some part of the manuscript. After using this tool/service, the author(s) reviewed and edited the content as needed and take(s) full responsibility for the content of the publication.

#### References

- Di Cesare, M., et al., World heart report 2023: Confronting the world's number one killer. World Heart Federation: Geneva, Switzerland, 2023.
- Martin, S.S., et al., 2024 Heart Disease and Stroke Statistics: A Report of US and
- 69 Global Data From the American Heart Association. Circulation, 2024. **149**(8): p. e347-
- e913.
- 3. Multiple Cause of Death 2018–2022 on CDC WONDER Database. National Center for
- Health Statistics: Hyattsville, MD, USA, 2023.
- 4. Mechanic, O.J., M. Gavin, and S.A. Grossman, Acute myocardial infarction. 2017.
- 5. Ojha, N. and A. Dhamoon, Myocardial Infarction. [Updated 2022 Aug 8]. StatPearls
- [Internet]. Treasure Island (FL): StatPearls Publishing, 2023.
- 876 6. Achenbach, S., et al., In-Plane Coronary Arterial Motion Velocity: Measurement with
- 877 *Electron-Beam CT.* Radiology, 2000. **216**(2): p. 457-463.
- 878 7. Mao, S., et al., Coronary artery motion in electron beam tomography. J Comput Assist
- 879 Tomogr, 2000. **24**(2): p. 253-8.
- 880 8. Lu, B., et al., Coronary artery motion during the cardiac cycle and optimal ECG
- triggering for coronary artery imaging. Invest Radiol, 2001. **36**(5): p. 250-6.
- 9. Ding, Z. and M.H. Friedman, Dynamics of Human Coronary Arterial Motion and Its
- Potential Role in Coronary Atherogenesis. Journal of Biomechanical Engineering,
- 884 2000. **122**(5): p. 488-492.
- 385 10. Johnson, K.R., et al., *Three-dimensional, time-resolved motion of the coronary arteries.*
- J Cardiovasc Magn Reson, 2004. **6**(3): p. 663-73.
- Shechter, G., J.R. Resar, and E.R. McVeigh, *Displacement and velocity of the coronary*
- arteries: cardiac and respiratory motion. IEEE Trans Med Imaging, 2006. 25(3): p.
- 889 369-75.
- 890 12. Tan, W., et al., Estimation of the displacement of cardiac substructures and the motion
- of the coronary arteries using electrocardiographic gating. Onco Targets Ther, 2013.
- **6**: p. 1325-32.
- 893 13. Chua, J.H., R. Nguyen, and A. Mahajan, Cardiac function and myocardial perfusion,
- in Perioperative Hemodynamic Monitoring and Goal Directed Therapy: From Theory
- to Practice, M. Cannesson and R. Pearse, Editors. 2014, Cambridge University Press:
- 896 Cambridge. p. 39-46.

- 14. Goodwill, A.G., et al., *Regulation of Coronary Blood Flow.* Comprehensive Physiology,
   2017. 7(2): p. 321-382.
- Weydahl, E.S. and J.E. Moore, *Dynamic curvature strongly affects wall shear rates in a coronary artery bifurcation model.* Journal of Biomechanics, 2001. **34**(9): p. 1189-
- 901 1196.
- 902 16. Prosi, M., et al., *Influence of curvature dynamics on pulsatile coronary artery flow in a* 903 *realistic bifurcation model.* J Biomech, 2004. **37**(11): p. 1767-75.
- Ramaswamy, S.D., et al., Fluid Dynamic Analysis in a Human Left Anterior Descending
   Coronary Artery with Arterial Motion. Annals of Biomedical Engineering, 2004.
- 906 **32**(12): p. 1628-1641.
- 907 18. Hasan, M., D.A. Rubenstein, and W. Yin, *Effects of cyclic motion on coronary blood*908 *flow.* J Biomech Eng, 2013. **135**(12): p. 121002.
- 909 19. Biglarian, M., et al., Computational investigation of stenosis in curvature of coronary 910 artery within both dynamic and static models. Computer Methods and Programs in 911 Biomedicine, 2020. **185**: p. 105170.
- 912 20. Zeng, D., et al., *Effects of cardiac motion on right coronary artery hemodynamics*. Ann Biomed Eng, 2003. **31**(4): p. 420-9.
- 914 21. Torii, R., et al., MR Image-Based Geometric and Hemodynamic Investigation of the 915 Right Coronary Artery with Dynamic Vessel Motion. Annals of Biomedical 916 Engineering, 2010. **38**(8): p. 2606-2620.
- 22. Zhou, M., et al., Wall shear stress and its role in atherosclerosis. Front Cardiovasc Med,
  2023. 10: p. 1083547.
- 919 23. Teng, Z., et al., Study on the association of wall shear stress and vessel structural stress 920 with atherosclerosis: An experimental animal study. Atherosclerosis, 2021. **320**: p. 38-921 46.
- Peiffer, V., S.J. Sherwin, and P.D. Weinberg, *Does low and oscillatory wall shear stress correlate spatially with early atherosclerosis? A systematic review.* Cardiovasc Res,
   2013. 99(2): p. 242-50.
- 925 25. Trayanova, N.A., J. Constantino, and V. Gurev, *Electromechanical models of the*926 *ventricles*. American journal of physiology. Heart and circulatory physiology, 2011.
  927 **301**(2): p. H279-H286.
- 928 26. Göktepe, S. and E. Kuhl, *Electromechanics of the heart: a unified approach to the*929 strongly coupled excitation-contraction problem. Computational Mechanics, 2010.
  930 **45**(2): p. 227-243.

- 931 27. Ahmad Bakir, A., et al., *A Multiphysics Biventricular Cardiac Model: Simulations With*932 *a Left-Ventricular Assist Device.* Frontiers in physiology, 2018. **9**: p. 1259-1259.
- 933 28. Regazzoni, F., et al., A cardiac electromechanical model coupled with a lumped-
- 934 parameter model for closed-loop blood circulation. Journal of Computational Physics,
- 935 2022. **457**: p. 111083.
- 936 29. Fedele, M., et al., A comprehensive and biophysically detailed computational model of
- 937 the whole human heart electromechanics. Computer Methods in Applied Mechanics
- 938 and Engineering, 2023. **410**: p. 115983.
- 939 30. Zingaro, A., et al., An electromechanics-driven fluid dynamics model for the simulation
- of the whole human heart. Journal of Computational Physics, 2024. **504**: p. 112885.
- 941 31. Zappon, E., et al., An integrated heart-torso electromechanical model for the
- simulation of electrophysiological outputs accounting for myocardial deformation.
- Computer Methods in Applied Mechanics and Engineering, 2024. **427**: p. 117077.
- 944 32. Fan, L., et al., Effects of Mechanical Dyssynchrony on Coronary Flow: Insights From
- a Computational Model of Coupled Coronary Perfusion With Systemic Circulation.
- 946 Frontiers in Physiology, 2020. 11.
- 947 33. Fan, L., et al., Optimization of cardiac resynchronization therapy based on a cardiac
- 948 electromechanics-perfusion computational model. Computers in Biology and
- 949 Medicine, 2022. **141**: p. 105050.
- 950 34. Fan, L., et al., Role of coronary flow regulation and cardiac-coronary coupling in
- 951 *mechanical dyssynchrony associated with right ventricular pacing.* Am J Physiol Heart
- 952 Circ Physiol, 2021. **320**(3): p. H1037-h1054.
- 953 35. Fan, L., et al., Transmural Distribution of Coronary Perfusion and Myocardial Work
- Density Due to Alterations in Ventricular Loading, Geometry and Contractility.
- 955 Frontiers in Physiology, 2021. 12.
- 956 36. Wang, Y. and X. Yin, Modelling coronary flow and myocardial perfusion by integrating
- 957 *a structured-tree coronary flow model and a hyperelastic left ventricle model.* Computer
- 958 Methods and Programs in Biomedicine, 2024. 243: p. 107928.
- 959 37. Zingaro, A., et al., A comprehensive mathematical model for cardiac perfusion.
- 960 Scientific Reports, 2023. **13**(1): p. 14220.
- 961 38. Wilson, N.M., A.K. Ortiz, and A.B. Johnson, *The Vascular Model Repository: A Public*
- 962 Resource of Medical Imaging Data and Blood Flow Simulation Results. J Med Device,
- 963 2013. **7**(4): p. 0409231-409231.
- 964 39. Vascular Model Repository. Available from: www.vascularmodel.com.

- 965 40. *3D Slicer*. Available from: <a href="http://www.slicer.org">http://www.slicer.org</a>.
- 41. Kikinis, R., S.D. Pieper, and K.G. Vosburgh, 3D Slicer: A Platform for Subject-Specific
- 967 Image Analysis, Visualization, and Clinical Support, in Intraoperative Imaging and
- 968 Image-Guided Therapy, F.A. Jolesz, Editor. 2014, Springer New York: New York, NY.
- 969 p. 277-289.
- 970 42. Palit, A., et al., Computational modelling of left-ventricular diastolic mechanics: Effect
- 971 *of fibre orientation and right-ventricle topology.* Journal of Biomechanics, 2015. **48**(4):
- 972 p. 604-612.
- 973 43. Kotadia, I., et al., Anisotropic Cardiac Conduction. Arrhythm Electrophysiol Rev,
- 974 2020. **9**(4): p. 202-210.
- 975 44. Wong, J. and E. Kuhl, Generating fibre orientation maps in human heart models using
- 976 Poisson interpolation. Comput Methods Biomech Biomed Engin, 2014. 17(11): p.
- 977 1217-26.
- 978 45. Piersanti, R., et al., Modeling cardiac muscle fibers in ventricular and atrial
- 979 electrophysiology simulations. Computer Methods in Applied Mechanics and
- 980 Engineering, 2021. **373**: p. 113468.
- 981 46. Bayer, J.D., et al., A novel rule-based algorithm for assigning myocardial fiber
- orientation to computational heart models. Ann Biomed Eng, 2012. 40(10): p. 2243-
- 983 54.
- 984 47. Streeter, D.D., Jr., et al., Fiber orientation in the canine left ventricle during diastole
- 985 *and systole.* Circ Res, 1969. **24**(3): p. 339-47.
- 986 48. Lombaert, H., et al., Human atlas of the cardiac fiber architecture: study on a healthy
- 987 *population.* IEEE Trans Med Imaging, 2012. **31**(7): p. 1436-47.
- 988 49. Nash, M.P. and A.V. Panfilov, *Electromechanical model of excitable tissue to study*
- 989 reentrant cardiac arrhythmias. Progress in biophysics and molecular biology, 2004.
- 990 **85**(2-3): p. 501-522.
- 991 50. Glukhov, A.V., et al., Transmural dispersion of repolarization in failing and nonfailing
- 992 *human ventricle*. Circ Res, 2010. **106**(5): p. 981-91.
- 993 51. Tusscher, K.H.W.J.T. and A.V. Panfilov, Modelling of the ventricular conduction
- 994 system. Progress in Biophysics and Molecular Biology, 2008. **96**(1): p. 152-170.
- 995 52. Sano, T., N. Takayama, and T. Shimamoto, *Directional difference of conduction velocity*
- 996 in the cardiac ventricular syncytium studied by microelectrodes. Circ Res, 1959. 7(2):
- 997 p. 262-7.

- 998 53. Eriksson, T.S.E., et al., *Influence of myocardial fiber/sheet orientations on left* 999 *ventricular mechanical contraction.* Mathematics and Mechanics of Solids, 2013.
- 1000 **18**(6): p. 592-606.
- 1001 54. Hooks, D.A., et al., Laminar Arrangement of Ventricular Myocytes Influences
- 1002 Electrical Behavior of the Heart. Circulation Research, 2007. 101(10): p. e103-e112.
- 1003 55. Holzapfel, G.A. and R.W. Ogden, Constitutive modelling of passive myocardium: a
- structurally based framework for material characterization. Philosophical Transactions
- of the Royal Society A: Mathematical, Physical and Engineering Sciences, 2009.
- **367**(1902): p. 3445-3475.
- 1007 56. Palit, A., et al., Passive diastolic modelling of human ventricles: Effects of base
- 1008 movement and geometrical heterogeneity. Journal of Biomechanics, 2017. 52: p. 95-
- 1009 105.
- 1010 57. Munneke, A.G., et al., A Closed-Loop Modeling Framework for Cardiac-to-Coronary
- 1011 *Coupling.* Frontiers in Physiology, 2022. **13**.
- 1012 58. Usyk, T.P., I.J. LeGrice, and A.D. McCulloch, Computational model of three-
- dimensional cardiac electromechanics. Computing and Visualization in Science, 2002.
- **4**: p. 249-257.
- 1015 59. Sankaran, S., et al., *Patient-Specific Multiscale Modeling of Blood Flow for Coronary*
- 1016 Artery Bypass Graft Surgery. Annals of Biomedical Engineering, 2012. **40**(10): p. 2228-
- 1017 2242.
- 1018 60. Kim, H.J., et al., Patient-specific modeling of blood flow and pressure in human
- 1019 *coronary arteries.* Ann Biomed Eng, 2010. **38**(10): p. 3195-209.
- 1020 61. Lock, J.E., Chapter 14 Cardiac Catheterization, in Nadas' Pediatric Cardiology
- 1021 (Second Edition), J.F. Keane, J.E. Lock, and D.C. Fyler, Editors. 2006, W.B. Saunders:
- 1022 Philadelphia. p. 213-250.
- 1023 62. Holzapfel, G.A. and R.W. Ogden, Constitutive modelling of arteries. Proceedings of
- the Royal Society A: Mathematical, Physical and Engineering Sciences, 2010.
- **466**(2118): p. 1551-1597.
- 1026 63. Sörnmo, L. and P. Laguna, Chapter 6 The Electrocardiogram—A Brief Background,
- in Bioelectrical Signal Processing in Cardiac and Neurological Applications, L.
- Sörnmo and P. Laguna, Editors. 2005, Academic Press: Burlington. p. 411-452.
- 1029 64. Pinnell, J., S. Turner, and S. Howell, *Cardiac muscle physiology*. Continuing Education
- in Anaesthesia Critical Care & Pain, 2007. 7(3): p. 85-88.

- 1031 65. Lang, R.M., et al., Recommendations for cardiac chamber quantification by
- echocardiography in adults: an update from the American Society of Echocardiography
- and the European Association of Cardiovascular Imaging. J Am Soc Echocardiogr,
- 1034 2015. **28**(1): p. 1-39.e14.
- 1035 66. Bathala, T.K., Chapter 6 Vascular Ultrasound, in Problem Solving in Cardiovascular
- 1036 Imaging, S. Abbara and S.P. Kalva, Editors. 2013, W.B. Saunders: Philadelphia (PA).
- 1037 p. 111-120.
- 1038 67. Gregg, D.E., Phasic blood flow and its determinants in the right coronary artery.
- American Journal of Physiology-Legacy Content, 1937. 119(3): p. 580-588.
- 1040 68. Barash, P.G., Clinical anesthesia. 2009: Lippincott Williams & Wilkins.
- 1041 69. Green, H.D., D.D. Gregg, and C.J. Wiggers, The phasic changes in coronary flow
- 1042 established by differential pressure curves. American Journal of Physiology-Legacy
- 1043 Content, 1935. **112**(4): p. 627-639.
- 1044 70. Algranati, D., G.S. Kassab, and Y. Lanir, Mechanisms of myocardium-coronary vessel
- interaction. Am J Physiol Heart Circ Physiol, 2010. 298(3): p. H861-73.
- 1046 71. Westerhof, N., et al., Cross-Talk Between Cardiac Muscle and Coronary Vasculature.
- 1047 Physiological Reviews, 2006. **86**(4): p. 1263-1308.
- 1048 72. Ramanathan, T. and H. Skinner, Coronary blood flow. Continuing Education in
- 1049 Anaesthesia Critical Care & Pain, 2005. **5**(2): p. 61-64.
- 1050 73. Shen, C., et al., Secondary flow in bifurcations Important effects of curvature,
- bifurcation angle and stents. Journal of Biomechanics, 2021. 129: p. 110755.
- 1052 74. Morbiducci, U., et al., Atherosclerosis at arterial bifurcations: evidence for the role of
- haemodynamics and geometry. Thrombosis and haemostasis, 2016. 115(03): p. 484-
- 1054 492.
- 1055 75. Zuin, M., et al., Role of secondary flows in coronary artery bifurcations before and after
- stenting: What is known so far? Cardiovascular Revascularization Medicine, 2023. 55:
- p. 83-87.
- 1058 76. Dean, W.R., XVI. Note on the motion of fluid in a curved pipe. The London, Edinburgh,
- and Dublin Philosophical Magazine and Journal of Science, 1927. 4(20): p. 208-223.
- 1060 77. Kok, F., R. Myose, and K.A. Hoffmann, Effects of planar and nonplanar curved flow
- paths on the hemodynamics of helical conduits for coronary artery bypass grafting: A
- numerical study. International Journal of Heat and Fluid Flow, 2020. **86**: p. 108690.
- 1063 78. Kao, H.C., Torsion effect on fully developed flow in a helical pipe. Journal of Fluid
- 1064 Mechanics, 1987. **184**: p. 335-356.

- Delestri, L.F.U., et al. Computational Analysis of The Effect of Cardiac Motion on Left
   Main Coronary Artery Hemodynamics. in 2022 Computing in Cardiology (CinC). 2022.
- 1067 80. Gijsen, F., et al., Expert recommendations on the assessment of wall shear stress in human coronary arteries: existing methodologies, technical considerations, and clinical applications. Eur Heart J, 2019. **40**(41): p. 3421-3433.